Identification of a novel and ancestral machinery involved in mitochondrial membrane branching in Trypanosoma brucei

Chloé Alexandra Morel, Corinne Asencio, Corinne Blancard, Bénédicte Salin, Etienne Gontier, Stéphane Duvezin-Caubet, Manuel Rojo, Frédéric Bringaud, Emmanuel Tetaud

HAL Id: hal-04300070
https://hal.science/hal-04300070

Preprint submitted on 22 Nov 2023

1 **Identification of a novel and ancestral machinery involved in**

2 **mitochondrial membrane branching in *Trypanosoma brucei***

3

4 **Short title:** Mitochondrial dynamics in trypanosomes

5

6 Chloé Alexandra Morel[1], Corinne Asencio[1], Corinne Blancard[2], Bénédicte Salin[2], Etienne

7 Gontier[3], Stéphane Duvezin-Caubet[2], Manuel Rojo[2], Frédéric Bringaud[1] and Emmanuel

8 Tetaud[1*]

9

10 [1] Univ. Bordeaux, CNRS, MFP, UMR 5234, F-33000, Bordeaux, France

11 [2] Univ. Bordeaux, CNRS, IBGC, UMR 5095, F-33000, Bordeaux, France

12 [3] Univ. Bordeaux, BIC, F-33000, Bordeaux, France

13

14 *Corresponding author: emmanuel.tetaud@u-bordeaux.fr

15 Tel: (+33) 0557574805

16 ***ABSTRACT***

17   African trypanosomes are eukaryotic parasites that exist in two main replicative

18 forms; the procyclic form in the midgut of the insect vector, the tsetse fly Glossina spp.

19 and the bloodstream form responsible for diseases in humans and cattle. Unlike most

20 other eukaryotes, where mitochondria continuously fuse and divide, trypanosome

21 mitochondria form a single and continuously interconnected network that only divides

22 during cytokinesis. The machineries governing mitochondrial remodeling and

23 interconnection, however, remain largely unknown. We characterize a dynamin-related

24 protein (DRP) from *T. brucei* (*Tb*DBF, previously called *Tb*MfnL) that depicts sequence

25 similarities with Opa1 and Mfn, mammalian DRPs involved mitochondrial fusion. We

26 showed that *Tb*DBF has closely related homologues in several organisms that are devoid

27 of Mfn and Opa1, such as eukaryotes from different phyla, prokaryotes and archaea.

28 *Tb*DBF is the first member of this new protein family to be functionally characterized. It

29 localizes to the mitochondrial periphery and, upon overexpression, induces a strong

30 increase in the interconnection and branching of mitochondrial filaments in a GTPase

31 dependent manner. Its overexpression also promotes a major increase in cellular and

32 mitochondrial volume and an increased consumption of the two major carbon sources

33 used by the parasite (glucose and proline), as well as ethanolamine, a precursor of

34 phosphatidyl-ethanolamine involved in membrane biogenesis and shaping. We propose

35 that mitochondrial *Tb*DBF is a component of an ancestral membrane remodeling

36 machinery that contributes to the formation of intermitochondrial connections.

INTRODUCTION

Trypanosoma brucei is a parasite responsible for African sleeping sickness as well as the related cattle disease Nagana, affecting sub-Saharan Africa. *T. brucei* is transmitted to mammals, its final host, by an insect vector: the tsetse fly. During the trypanosome life cycle, the parasite exists in at least two replicative forms; the procyclic form (PCF), transmitted by the tsetse fly Glossina spp., and the bloodstream form (BSF) responsible for diseases in vertebrates. The pathogenic trypanosomes have a single mitochondrion, unlike most other eukaryotes that contain numerous ones (1). Trypanosome's mitochondrion is highly elongated and reticulated and its genome (mitochondrial DNA) is restricted to a specific structure at the basis of the flagellum known as kinetoplast (kDNA). During the trypanosome life cycle and its adaptation to different hosts and environments, the shape of its mitochondrial compartment undergoes spectacular changes that reflect its functional plasticity. Indeed, the mitochondrion of this parasite exists in at least two major forms: (i) the fully active and developed one characteristic for the PCF that harbors the oxidative phosphorylation complexes (OXPHOS) for energy production (2, 3) and (ii) the functionally less active and morphologically reduced form found in the bloodstream, with energy produced exclusively through glycolysis since OXPHOS is repressed (4). These modifications correlate with the adaptation of the parasite to the glucose-rich blood of a mammalian host and the proline-rich hemolymph and tissue fluids of the blood-feeding tsetse fly (5). Studies in mammals and in yeast having unraveled tight links between mitochondrial bioenergetics, morphology and dynamics (6-8), it is tempting to assume that such close relationships not only regulate mitochondrial function and energy metabolism, but also the life cycle and pathogenic potential of trypanosomes. However, in contrast to fungi and metazoa, where mitochondrial morphology and fusion/fission dynamics have been thoroughly characterized (9, 10), little is known about the morphology and dynamics of mitochondria in trypanosomes.

In most eukaryotes, mitochondria are very dynamic, alternating between two major events; fusion and fission. Mitochondrial dynamics allows to maintain mitochondrial

66   morphology, distribution and size (7). The main proteins involved in these events are

67   large GTPase belonging to the dynamin family. The main GTPase responsible for

68   mitochondrial fission in yeast and mammalian cells is Dnm1/Drp1, a soluble protein

69   which is recruited to mitochondrial and peroxisomal membranes to exert its function (11,

70   12). Mammalian mitochondrial fusion requires fusion of outer mitochondrial membrane

71   (OMM) followed by fusion of inner mitochondrial membrane (IMM) which is carried out by

72   mitofusins 1 and 2 (Mfn1 and Mfn2) and optic atrophy 1 (Opa1), respectively (13, 14).

73   Alteration in one of these processes and of the equilibrium between them provokes

74   mitochondrial fragmentation or hyperfusion (11, 15) and is linked to diseases, notably

75   neuropathies (16).

76   Mitochondrial fusion and fission in trypanosomes have been poorly investigated to

77   date. Unlike mammalian and yeast cells, fusion has not been directly observed (17, 18),

78   but indirect evidence for mitochondrial fusion came 25 years ago from *in vivo* genetic

79   exchange of mtDNA (19). Another indication of fusion stems from the observation that

80   the mitochondrial fragmentation provoked by the overexpression of mammalian Bax in

81   trypanosomes is reversible (20) and from the observation that, in BSF, the mitochondrial

82   network mostly grows from two areas where loops and branches eventually merge to

83   build a complex network (17). Available evidence indicates that mitochondrial fission is

84   not an endogenous/spontaneous process (17, 18) but it has to be artificially induced to

85   be observed (20, 21) and appears restricted to parasite division (18, 21). More recently,

86   expression, in the mitochondrial matrix of trypanosome, of a putative dynamin from

87   giant viruses has shown remodeling of the mitochondrion into a simple tubular structure,

88   supporting that mitochondrial fission occurs in this parasite (22). The absence of

89   spontaneous, ongoing or continuous fission could explain the unique tubular and

90   reticulated structure of the parasite mitochondrion, resembling that observed in yeast or

91   mammalian mutants devoid of fission (23, 24). Finally, a recent study of the

92   mitochondrial structure in another trypanosomatid (*Crithidia fasciculata*), revealed slow

93   and discrete fission and fusion events during the cell cycle, suggesting that fusion/fission

94   machineries must exist in trypanosomatids (25).

95   Two decades of research have revealed that numerous mitochondrial fusion and
96   fission factors appear conserved in fungi and mammals with non-neglectable differences
97   (7). In plants, mitochondria fuse and divide, but factors directly involved in fusion have
98   not been clearly identified until now, suggesting the existence of a different fusion
99   machineries (26, 27). So far, only one dynamin-related protein (DRP), *Tb*Dlp, has been
100   described and studied in *T. brucei*: its ablation impairs mitochondrial division and
101   endocytosis and leads to cytokinesis arrest (21, 28). *Tb*Dlp thus appears to be the
102   functional homolog of Drp1/Dnm1 in mammals and yeast, but its fission activity seems
103   restricted to the cytokinesis (21). Another putative DRP displaying some similarity to
104   mitofusins (*Tb*MFNL, Tb927.7.2410) has been reported to influence the mitochondrial
105   shape (29). Its down-regulation led to a highly fenestrated mitochondrial network,
106   suggesting that, despite its name, it plays a role in mitochondrial fission (29). To date,
107   no protein has been involved in mitochondrial fusion in trypanosomes.

108   In this study, we characterized the trypanosome DRP named *Tb*MFNL (29). We
109   show that this DRP shows a strong similarity with a family of eukaryotic, prokaryotic and
110   archaeal proteins that is absent from all organisms expressing Mfn or Opa1 homologues
111   (fungi and mammals) and from plants, suggesting that it belongs to an ancestral
112   membrane remodeling machinery. We show that it localizes to mitochondrial membranes
113   and is able to modulate mitochondrial branching and shape. Its deletion does not alter
114   mitochondrial morphology or distribution but its overexpression increases the size and
115   branching of its mitochondrial compartment in a GTP-dependent manner. Taken
116   together, our findings reveal that mitochondrial branching in trypanosomes is modulated
117   by a member of a novel and ancestral membrane remodeling machinery that we have
118   named *Tb*DBF for *Trypanosoma brucei* Dynamin-related Branching Factor.

RESULTS

1 - Identification and sequence analysis of TbDBF

121   To identify potential fusion players, we started our search by careful re-examination

122 of trypanosome genomic and proteomic databases for proteins showing sequence

123 homology to known fusion factors (Opa1/Mfn1/2). We were only able to identify the

124 previously reported dynamin-related protein *Tb*MFNL (Tb927.7.2410) (29), that displays

125 some similarities with both mammalian fusion factors of the inner (Opa1) or outer

126 membrane (Mfn2) with 21 and 23 % of sequence identity, respectively (**Figure 1, S1**

127 **and Table S1**). Analysis of its sequence identified several motifs and domains found in

128 other mitochondrial DRPs. Indeed, its N-terminal sequence displays a potential

129 mitochondrial targeting signal (MTS) with potential cleavage sites (**Figure S1**), followed

130 by a GTPase domain with conserved G1 to G4 motifs and, in its C-terminal region, two

131 consecutive transmembrane domains (TM) (**Figure 1 and S1**). Interestingly, the MTS

132 points to inner membrane targeting (such as the inner membrane fusion factor Opa1

133 localizing to the intermembrane space). In contrast to Opa1, that carries an N-proximal

134 TM domain mediating inner membrane anchoring, no transmembrane domain was

135 identified following the MTS, suggesting that it is not an Opa1 counterpart. The overall

136 structure and domain organization of the protein displays more similarity to human Mfn

137 (**Figure 1**) with two C-proximal transmembrane domains (TMs) that are reminiscent of

138 the targeting to the outer mitochondrial membrane of Mfn. However, the presence of a

139 N-terminal MTS makes it unlikely to be located in the outer membrane like Mfn in

140 mammals. Altogether, these data suggest that the protein named *Tb*MFNL (29) is not a

141 homolog of fusion factors Opa1 or Mfn.

142   We therefore investigated whether this DRP could be conserved in other organisms.

143 As expected, it is well conserved throughout the *kinetoplastida* order (**Figure S2 and**

144 **Table S1** for some examples) but, surprisingly, we identify homologous proteins, with

145 high similarity over the whole sequence, in many eukaryote lineages (mainly in the SAR

146 clade *Stramenopiles* and *Alveolata*) (**Figure 2A, S3 and Table S1**) but never in

147 *Opisthokonta* (clade including fungi and mammals) or in plants. Unexpectedly, we also

148 identified many similar sequences in bacteria, mainly in the PVC group and in

149 proteobacteria (**Figure 2A**). Finally, a sequence was also identified in *Archaea*, revealing

150 that, unlike Opa1 and Mfn proteins, the proteins of this family are conserved in all the

151 three domains of life (**Figure 2A, S3 and Table S1**). Remarkably, we could not identify

152 sequences corresponding to Opa1 and Mfn in any of these organisms, the only sequences

153 identified being restricted, as anticipated, to the well-conserved GTPase domain.

154 Phylogenetic analysis was carried out using the amino acid sequences of the proteins and

155 a comprehensive tree based on sequence alignment is shown in **Figure 2B**. Structural

156 analysis of several of these identified proteins, show again a very conserved structural

157 organization on the whole sequence (**Figure 2C and S3**). Indeed, apart from the

158 obvious absence of the MTS in prokaryotes, the general structure and domain

159 organization are extremely well preserved (**Figure 2C**). Altogether, our analysis shows

160 that these proteins form a phylogenetic group that is clearly separated from the well-

161 known fusion and fission dynamins of fungi and mammals and of *Np*BDLP, its closest

162 bacterial homologue (**Figure 2B**). As these DRPs are conserved throughout the living

163 world, but not in fungi, mammals, and plants, it is tempting to speculate that they

164 represent a component of a novel and ancestral machinery involved in membrane

165 dynamics. Their belonging to a protein family different from that of mitofusins and the

166 functional characterization described below led us to rename this DRP *Tb*DBF (for

167 *Trypanosoma brucei* Dynamin-related Branching Factor).

168

169 ***2 - TbDBF is localized in the mitochondrion***

170   Interrogation of the TrypTag database (cellular localization of trypanosome proteins

171 (30)) with the *Tb*DBF sequence (Tb927.07.2410) reveals mitochondrial localization for a

172 C-terminal GFP-tagged version and a cytoplasmic, flagellar and nuclear lumen

173 localization for an N-terminal GFP tagged construct. One potential explanation for this

174 apparent discrepancy is that adding an N-terminal GFP sequence in front of a

175 mitochondrial targeting sequence (MTS) is expected to perturb its addressing and

176 therefore does not allow to conclude on its localization. To confirm the subcellular

7

177 localization of *Tb*DBF in *T. brucei*, we added a C-terminal 10xHA tag (to avoid disruption

178 of mitochondrial targeting) to endogenous *Tb*DBF (*Tb*DBF::10HA) in both PCF and BSF

179 using the pPOTV7 vector series (31) (**Figure 3A**) and verified that the tag has no impact

180 on cell growth (**Figure S4**). It should be noted that the slight variation in growth

181 observed between the wild-type and the tagged strain could be due to the difference

182 between a non-clonal (wild-type) and clonal (*Tb*DBF::10HA) population. Expression of

183 *Tb*DBF::10HA was confirmed by western-blot with anti-HA antibody in PCF and BSF (**Figure**

184 **3B**). The protein is about 2-fold more expressed in PCF than BSF which is in agreement

185 with the data obtained by SILAC analysis for this protein (32). The localization of the

186 *Tb*DBF protein was studied in PCF by immunofluorescence using threonine

187 dehydrogenase (Tdh, (33)) as a mitochondrial matrix marker (**Figure 3C**). *Tb*DBF::10HA

188 and Tdh clearly colocalized in the mitochondrial compartment, but *Tb*DBF depicted a less

189 homogeneous mitochondrial distribution (**Figure 3C, Anti-HA/Merge**). We also

190 addressed, by immunofluorescence, *Tb*DBF subcellular localization in BSF. For technical

191 reasons (Tdh antibody do not react in bloodstream and the lack of primary antibody of

192 non-murine origin), we could not perform a colocalization of the *Tb*DBF::10HA protein with

193 a mitochondrial protein. However, we performed a parallel labeling of the mitochondria,

194 with an antibody directed against the mitochondrial Hsp60 or against the HA-tag. Under

195 these conditions, we observe a tubular structure characteristic of the BSF mitochondrion

196 both for *Tb*DBF and Hsp60 (**Figure 3D**). The overall modular organization of *Tb*DBF

197 previously described and its subcellular localization confirm that *Tb*DBF is a mitochondrial

198 protein.

199

200 ***3 – Inactivation and silencing of TbDBF does not alter mitochondrial shape***

201 Live microscopy of yeasts and cultured mammalian cells has revealed that

202 mitochondrial morphology is continuously remodeled by antagonizing fission and fusion

203 reactions (15, 34). Under normal conditions, the fusion/fission balance is established in

204 favor of fusion and the mitochondria appear filamentous. Inhibition of fusion leads to

205 mitochondrial fragmentation by ongoing fission (15) and reversely enhancing fusion leads

206 to hyperfused mitochondria with increased branching and interconnection (11). In
207 contrast, trypanosomes show a single permanently branched and interconnected
208 mitochondrion, with very few mitochondrial fission events reported, which appear to be
209 restricted to cell division and especially cytokinesis (18, 21).

210   To investigate the role of *Tb*DBF, we first inactivated the gene encoding *Tb*DBF by
211 CRISPR/Cas9 (35) with an optimized protocol (see Materials and Methods). Both *Tb*DBF
212 alleles were inactivated by integration of a puromycin resistance marker cassette into
213 both PCF and BSF cells (**Figure 4A**). Cloned parasites were analyzed by PCR to select
214 cell lines carrying PAC insertions in both *Tb*DBF alleles (*Tb*DBF$^{-/-}$) (**Figure 4B**). No
215 significant impact on cell growth was observed in these PCF and BSF null-mutants over a
216 period of 7 days compared to wild-type cells. We infer that the slight variation in growth
217 observed between the wild-type and the inactivated strain reflects the difference
218 between a non-clonal (wild-type) and clonal (*Tb*DBF$^{-/-}$) population (**Figure S4**). To
219 investigate potential impact of *Tb*DBF$^{-/-}$ on mitochondrial shape, we labeled PCF
220 mitochondria with rhodamine-123 staining and analyzed mitochondrial shape in living
221 cells. Since BSF were too mobile to obtain focused images with rhodamine 123, we
222 stained mitochondria in fixed cells by immunofluorescence with mitochondrial Hsp60
223 antibodies. In both PCF and BSF, no significant difference in the structure of the *Tb*DBF$^{-/-}$
224 mitochondrion was observed (**Figure 4C and 4E**). To confirm that this strategy leads to
225 *Tb*BDF inactivation, we repeated this process in a strain endotagged with a C-terminal
226 3xTy1 tag in order to follow the expression of the protein by western-blot (**Figure S5/A-**
227 **D**). Two separate inactivations were performed, one by inserting the puromycin
228 resistance gene as before (**Figure S5E-G**) and the other one by deleting part of the gene
229 (**Figure S5H-J**). In both cases, the protein was not detected in the inactivated clones
230 and no modification of the mitochondrial structure was observed (**Figure S5G/J**).

231   In order to detect and quantify discrete modifications of the mitochondrial shape
232 that may escape detection upon qualitative visual analysis, we developed an ImageJ
233 macro (**Supplemental MMS1**) for the automatic analysis of the obtained images, which
234 allows quantification of mitochondrial junctions (**Figure 4D**). This allowed us to establish

235   that the number of mitochondrial junctions is equivalent in *Tb*DBF^{-/-} and wild-type PCF

236   cells (8.5±4.9 vs 9.4±4.3) confirming the qualitative analysis of the microscopy images

237   (**Figure 4C**). These findings regarding the consequences of *Tb*DBF inactivation in PCF

238   and BSF are not in line with a previous report describing a highly fenestrated

239   mitochondrial network consecutive to a partial but significant inhibition (70%) of *Tb*DBF

240   (*Tb*MFNL) expression by RNAi in BSF (29). To exclude that the divergence arose from the

241   different inactivation and silencing strategies, we conditionally down-regulated

242   expression of *Tb*DBF using a stem-loop RNAi construct. This approach led to a significant

243   reduction (~70%) of the expression of endogenously tagged *Tb*DBF::10HA in PCF (as

244   observed in BSF (29)), but this was not paralleled by a modification of mitochondrial

245   shape (**Figure S6A-C**). Since mitochondrial fenestration upon *Tb*MFNL/*Tb*DBF silencing

246   was observed in BSF (29) we decided to repeat the experiment using the same strain (*T.*

247   *brucei* 427 BSF), the same RNAi system (p2T7-177) and the same sequence used for

248   down-regulation (29). As previously reported (29), we observed a significant reduction of

249   *Tb*DBF expression (~80% after 4 days) of the endogenously tagged *Tb*DBF::3HA in BSF

250   (**Figure S6D-F**) that was not accompanied by mitochondrial shape modifications (**Figure**

251   **S6G**). In our hands, neither inactivation nor silencing of *Tb*MFNL/*Tb*DBF alters

252   mitochondrial morphology or induces a fenestration phenotype. At present, we ignore the

253   reasons for the discrepancy with the results reported by Vanwalleghem et *al*. (29).

254

255   *4 - TbDBF overexpression increases mitochondrial branching in a GTP-*

256   *dependant manner*

257   We also investigated the possible role of *Tb*DBF by conditionally expressing a C-

258   terminally-tagged (3xTy1) *Tb*DBF ([oe]*Tb*DBF::3Ty1) in PCF (**Figure 5A**). Expression was

259   confirmed by western-blot analysis after 3 to 5 days of tetracycline induction (**Figure**

260   **5B**). Rhodamine-123 staining showed that wild-type and non-induced [oe]*Tb*DBF::3Ty1 cells

261   harbor the expected reticulated mitochondrial structure, while the mitochondrion appears

262   significantly more reticulated and branched in induced [oe]*Tb*DBF::3Ty1 cells (**Figure 5C and**

263   **Figure S7**). For a more precise and quantitative description of the branching phenotype,

we used our ImageJ macro allowing quantification of mitochondrial junctions. After 5 days of induction, the average number of mitochondrial junctions appeared more than 2-times higher in induced ^{oe}TbDBF$_{::3Ty1}$ cells compared to non-induced or wild type cells (**Figure 5G**). In order to estimate the level of TbDBF overexpression achieved in *T. brucei* PCF, we repeated this experiment with cells expressing endogenously 3Ty1-tagged TbDBF (TbDBF$_{::3Ty1}$, clone 2A11; **Figure S5A-D**). Western-blot analysis revealed that upon induction, exogenous TbDBF$_{::3Ty1}$ protein is well overexpressed relative to its endogenous expression and induces alterations of mitochondrial shape (**Figure S8A/B**). It is also noteworthy that the expression of TbDBF without the C-terminal 3Ty1 tag induces the same phenotype as the tagged TbDBF, confirming that the phenotype is not due to the use of a C-terminal tag (**Figure S8A/B**). These data clearly demonstrate that overexpression of TbDBF stimulates intermitochondrial connections.

All Dynamin-like proteins possess a GTP-binding domain that binds and hydrolyzes GTP and mutations in the highly conserved domains interacting with GTP provoke dynamin-dysfunction by lowering GTP-binding and hydrolysis efficiency. To determine whether TbDBF requires a functional GTPase domain to function, the key lysine 141 in the highly conserved G1 motif was converted to alanine, a mutation (K141A) significantly reducing GTP-binding of dynamins in other organisms (36-38). The K141A mutation was introduced into the sequence of TbDBF tagged with a C-terminal 3Ty1 (^{oe}TbDBFK141A$_{::3Ty1}$, **Figure 5D**). Expression was confirmed by western-blot analysis after 3 to 5 days of tetracycline induction (**Figure 5E**) and overexpression of TbDBFK141A$_{::3Ty1}$ was also confirmed as the wild-type TbDBF$_{::3Ty1}$ (**Figure S8A**). The mutated protein localized to the mitochondria (**Figure 6D**), as expected, but did not alter mitochondrial shape (**Figure 5F, Figure S7**) nor the number of mitochondrial junctions (**Figure 5G**). This clearly demonstrates that TbDBF is a dynamin related protein that relies on a functional GTPase domain to modulate mitochondrial branching in trypanosomes.

5 - Submitochondrial localization of TbDBF

293   The localization of overexpressed *Tb*DBF was also analyzed by immunofluorescence.

294   The overexpressed *Tb*DBF::3Ty1 co-localized with Tdh in mitochondria (**Figure 6A-d5.i**),

295   as previously described for the endogenous protein (**Figure 3C**). Analysis of

296   mitochondrial shape by immunofluorescence confirmed that overexpression of *Tb*DBF is

297   linked to the appearance of hyper-reticulated mitochondrion (**Figure 6A-d5 .i**), as

298   previously observed in living, rhodamine-123 labeled cells (**Figure 5C**). For more precise

299   *Tb*DBF localization, we performed Ultrastructure Expansion Microscopy (U-ExM), which

300   increases the size of a sample while preserving its ultrastructure (39, 40). By this

301   approach, we show that both ^{oe}*Tb*DBF::3Ty1 (**Figure 6B**) and the endogenous *Tb*DBF::10HA

302   (**Figure 6C**) have a different distribution from the matrix marker (Tdh) and localizes to

303   the mitochondrial periphery. In addition, as already noticed with standard

304   immunofluorescence microscopy (**Figure 3C**), *Tb*DBF depicts a non-continuous, punctate

305   distribution within the membrane as compared to the matrix protein Tdh. These findings

306   suggest an association of the *Tb*DBF protein with mitochondrial membranes. We then

307   investigated the effect of *Tb*DBF expression in the BSF form, where the mitochondrial

308   compartment is smaller and composed of shorter and less interconnected mitochondria.

309   Overexpression of ^{oe}*Tb*DBF::3Ty1 was monitored by western-blot (**Figure 6E**), but unlike

310   PCF, the mitochondrial structure (labeled here with mitochondrial Hsp60) was not at all

311   altered, remaining tubular and slightly reticulated like in wild-type cells (**Figure 6F**).

312   Induction over a longer period (up to 21 days) did not show mitochondrial alterations.

313   The localization of the wild-type *Tb*DBF and mutant *Tb*DBF (K141A) was also

314   investigated by electron microscopy (EM) and immunogold-labeling using an anti-Ty1

315   antibody. After induction and immunogold-labeling, both proteins are clearly localized in

316   the mitochondrion (**Figure S9A3/B3**) as compared to controls with non-induced cells

317   (**Figure S9A1/B1**), which is also confirmed by gold-particles quantification (**Figure**

318   **S9D**).

319

320   *6 - Mitochondrial targeting and membrane anchoring of TbDBF*

321   To investigate the mechanisms ensuring mitochondrial targeting of *Tb*DBF, we first

322   addressed the two domains that may determine *Tb*DBF localization: (i) the N-terminal

323   MTS that could mediate inner membrane targeting and intermembrane space localization

324   (as the MTS of Opa1), and (ii) the C-proximal/terminal TMs that could mediate outer

325   membrane anchoring (as the TMs of Mfn). To investigate their capacity to target proteins

326   to mitochondria, we fused the MTS domain, or the two transmembrane domains of

327   *Tb*DBF, to GFP (**Figure 7A**). Fusion of the MTS at the N-terminus of GFP (MTS::GFP) fully

328   addressed GFP to the mitochondria (**Figure 7A**). Interestingly, the size of MTS::GFP

329   revealed by Western-blot is identical to that of cytosolic GFP without MTS (**Figure 7B**),

330   indicating that the predicted MTS maturated by Matrix Processing Peptidase (MPP)

331   (**Figure S1**) was cleaved upon import of MTS::GFP across the inner membrane. It is to

332   note that ^{oe}*Tb*DBF::3Ty1 and ^{oe}*Tb*DBFK141A::3Ty1 showed the same apparent size as

333   ^{oe}*Tb*DBFΔMTS::3Ty1 by western-blot analyses, indicating that the MTS is also cleaved in its

334   natural context (**Figure 7C**) and thus, at least the N-terminus of *Tb*DBF is imported into

335   the matrix. We then investigated the addition of the 2 C-proximal transmembrane

336   domains at the C-terminal extremity of GFP (GFP::TM). As expected, a size shift

337   corresponding to the addition of transmembrane domains is observed by western-blot

338   (**Figure 7B**). However, in contrast to MTS::GFP, the GFP::TM was not targeted to

339   mitochondria, but to unknown distinct structures, possibly membrane or ER as well as

340   the flagellum which is different from a cytosolic labeling (see GFP alone) or from a

341   mitochondrion labeling (here revealed with the anti-Tdh antibody) (**Figure 7A and**

342   **Figure S10**). Their inability to mediate mitochondrial targeting shows that the TMs of

343   *Tb*DBF do not represent mitochondrial targeting determinants like those targeting

344   mitofusins to the mitochondrial outer membrane. Their capacity to target GFP from the

345   cytosol to other organelles, suggests that they have the capacity to mediate membrane

346   anchoring. It is probable that this membrane-anchoring function is exerted within

347   mitochondria, upon MTS-mediated targeting of *Tb*DBF.

348   In order to further characterize the role and relevance of these domains on *Tb*DBF

349   localization   and   function,   we   expressed   tagged   *Tb*DBF-mutants   without   MTS

350 (^{oe}TbDBFΔMTS$_{::3Ty1}$) or TMs (^{oe}TbDBFLΔTM$_{::3Ty1}$) in PCF using tetracycline-induction

351 (**Figure 7D and 7G**). Conditional overexpression of both recombinant TbDBF was

352 confirmed by western blot, after 3 days to 5 days of induction (**Figure 7E/7H/S8**). In

353 contrast to ^{oe}TbDBF$_{::3Ty1}$, a significant proportion of ^{oe}TbDBFΔMTS$_{::3Ty1}$ doesn't colocalize

354 with Tdh revealing that the N-terminal MTS is indeed required for proper mitochondrial

355 targeting of TbDBF (**Figure 7F, Figure S10**). Interestingly, the labeling observed for

356 ^{oe}TbDBFΔMTS$_{::3Ty1}$ is somewhat similar to the labeling of GFP$_{::TM}$ (**Figure 7A/F/S10**),

357 suggesting unspecific membrane anchoring by C-proximal TMs. The fact that part of

358 ^{oe}TbDBFΔMTS$_{::3Ty1}$ still remained close to Tdh signal may show that the ΔMTS mutant is

359 also anchored to mitochondrial membranes. To analyze the localization of

360 ^{oe}TbDBFΔMTS$_{::3Ty1}$ with more precision, we performed electron microscopy analysis with

361 anti-Ty1 antibody. We observed a dual localization of ^{oe}TbDBFΔMTS$_{::3Ty1}$, and gold-

362 particles quantification revealed that 60% of ^{oe}TbDBFΔMTS$_{::3Ty1}$ is located outside of the

363 mitochondrion and 40% inside or close to the mitochondrion membranes (**Figure**

364 **S9C/D**). MTS is therefore important for the correct localization of TbDBF, but without it,

365 the protein is partially able to localize to membranes. We further observed that

366 overexpression of ^{oe}TbDBFΔMTS$_{::3Ty1}$ does not alter mitochondrial structure, indicating

367 that its proper, MTS-mediated, mitochondrial localization is essential for TbDBF-function

368 (**Figure 7F/Anti-Tdh and Figure S8**). We then investigated the relevance of the C-

369 proximal TMs of TbDBF by overexpressing a version truncated for the TM

370 (^{oe}TbDBFΔTM$_{::3Ty1}$, **Figure 7G**) and analyzed the mitochondrial shape and their

371 localization by immunofluorescence (**Figure 7I**). ^{oe}TbDBFΔTM$_{::3Ty1}$ is also well over-

372 expressed (**Figure 7H and Figure S8**) and perfectly colocalizes with the mitochondrial

373 marker, like $_{MTS::}$GFP. This confirms that the N-terminal MTS sequence is sufficient for

374 mitochondrial targeting of TbDBF. However, no modification of the mitochondrial shape

375 was observed (**Figure 7E3 and Figure S8**) demonstrating that the transmembrane

376 domains are required for proper function. Altogether, our data show that TbDBF is

377 targeted to mitochondria by an N-terminal MTS and that C-proximal TMs are required for

378 proper function. We infer that TMs probably mediate membrane anchoring and the

379 establishment of proper membrane topology.

380

381 **7 – Impact of TbDBF overexpression on parasite morphology/biology**

382   We then decided to characterize *Tb*DBF activity and intermitochondrial branching

383 with higher resolution. To this end, we used as serial block face scanning electron

384 microscopy (SBF-SEM), an approach allowing to characterize the overall structure of

385 membranes and organelles within the entire cell volume (18). With this technique,

386 hundreds of images are collected to perform a 3D reconstruction of the whole cell, as

387 well as spatial organization of the individual organelles within the cell. Four to five wild-

388 type and ^{oe}*Tb*DBF$_{::3Ty1}$ PCF cells were reconstructed in 3D, with a particular emphasis on

389 the mitochondrion, the nucleus, the flagellar pocket and the cell outline. We have not

390 been able to correctly identify the kinetoplast DNA on the electron microscopy images,

391 thus preventing its 3D reconstruction. However, since kDNA is in close contact with the

392 flagellar pocket, it is easy to position it. Other organelles (glycosomes, acidocalcisomes,

393 golgi, flagellum, etc.) are not represented either in order to not overload the 3D

394 representation. As expected, wild-type PCF cells showed a reticulated mitochondrion

395 along the whole cell (**Figure 8A/C**), a rather central nucleus and the flagellar pocket on

396 the posterior side. The length of the wild-type and ^{oe}*Tb*DBF$_{::3Ty1}$ cells, varies between

397 20.4±3.3 and 23±4.7 μm, respectively. As observed by fluorescence microscopy,

398 ^{oe}*Tb*DBF$_{::3Ty1}$ mitochondrion showed more areas with stronger reticulation (**Figure 8B/D,**

399 **indicated by arrows**). Unexpectedly, in some cells this reticulation is even more

400 prominent at the edges of the flagellar pocket, where the kDNA is located, as illustrated

401 in **Figure 8B/D**, an observation that we had not identified by immunofluorescence

402 microscopy approaches. This hyper-reticulated structure (leaving a few gaps in the

403 mitochondrion) forms a globular structure and probably encapsulates the kDNA (**Figure**

404 **8D, indicated by small arrows**). This structure has been already described in BSF and

405 called kDNA pocket (17), but this structure is even more prominent in the ^{oe}*Tb*DBF$_{::3Ty1}$

406 cells. It should be noted that the 3D reconstruction of ^{oe}*Tb*DBF$_{::3Ty1}$ cells required the

15

407 analysis of more slices in order to have a whole cell, suggesting a larger volume of the

408 cell with a width at the nucleus of ~3.96±1.19 μm for ^{oe}TbDBF$_{::3Ty1}$ and ~2.51±0.28 μm

409 for wild-type cells, but no modification in the length of the parasite was observed. Wild-

410 type cells exhibit a cell volume around 53.5±6.6 μm^3, which are quite similar to the

411 volume measured in the different stages of the BSF cell cycle (cell 31-61 μm^3, (18)

412 **Figure 8E**). As anticipated, PCF mitochondrial volume is nearly doubled (4.9±1 μm^3)

413 compared to the mitochondrial volume of BSF (1.1-3 μm^3) (17, 18). As expected,

414 mitochondrial volume in cells overexpressing TbDBF$_{::3Ty1}$ is almost doubled by

415 comparison to wild-type cells (**Figure 8E**) and surprisingly the whole cell volumes was

416 also increased ~1.7-fold in ^{oe}TbDBF$_{::3Ty1}$ cells (**Figure 8E**).

417　　　On the other hand, and as presented in the introduction, the shape of the

418 mitochondrion undergoes spectacular changes during the life cycle of the parasite,

419 reflecting adaptation to different environments. These adaptations are also accompanied

420 by a profound change in their metabolism. We therefore investigated whether and how

421 an alteration of the mitochondrial structure affects the metabolism of the parasite. To

422 address this, we screened for the use of 119 different carbon and nitrogen sources in

423 parasites overexpressing or not TbDBF. Two carbon sources, D-glucose and L-proline

424 (**Figure 9 and Figure S11,** n°14/114), are significantly more consumed/used in

425 ^{oe}TbDBF$_{::3Ty1}$ cells compared to non-induced cells, suggesting that modifications of the

426 mitochondrial structure require increased energy consumption or to the opposite, that

427 mitochondrial shape restructuring impacts metabolism. Interestingly, ethanolamine is

428 also significantly more consumed/used in ^{oe}TbDBF$_{::3Ty1}$ cells (**Figure 9 and Figure S11,**

429 n°61). This molecule is a precursor of phosphatidylethanolamine, an important

430 component of mitochondrial membranes (41), which in line with the observed increase in

431 mitochondrial complexity. Altogether these data suggest that ^{oe}TbDBF$_{::3Ty1}$ cells need

432 more energy and metabolic precursors, from increased catabolism of carbon sources, to

433 fuel the increased membrane biosynthesis.

434

DISCUSSION

We have identified a novel and ancestral DRP family whose first representative, *Tb*DBF, has been characterized in the protozoan parasite *T. brucei*. We have demonstrated that *Tb*DBF localizes to the mitochondrial periphery and is able to increase mitochondrial interconnectivity in a GTPase-dependent manner. Its overexpression also induces modifications in energy metabolism in the parasite, as well as membrane biogenesis and shaping. We propose that mitochondrial *Tb*DBF may mediate and/or enhance fusion.

Membrane fusion and fission are often controlled by proteins of the dynamin superfamily (DRP) (42, 43). These proteins consistently have a GTPase domain and contain domains required for membrane binding and oligomerization. In trypanosomes, only DRPs involved in fission have been characterized, and no fusion proteins similar to those of yeasts and mammals have been identified so far. This may suggest that trypanosome mitochondria fuse via a machinery that differs from that characterized in yeasts and mammals. Of note, the situation is similar in plants, where no fusion protein similar to known fusion factors has been identified until now. Indeed, the search for homologous sequences to *Tb*DBF allowed us to identify close DRP homologs in several eukaryotic phyla lacking Mfn and Opa1, the fusion factors of metazoan and fungi. Unlike Mfn and Opa1, that have few homologues in some prokaryotes (cyanobacterial BDLP), homologues of *Tb*DBF were also identified in numerous bacterial phyla and even in archaea. These data point to the existence in these organisms of a novel machinery involved in membrane fusion, shaping and/or remodeling that is not present in *Opisthokonta* and *Plantae* but still present in numerous prokaryotes. While studies of yeast and mammalian DRPs provide information about their functions and structures, little is known about bacterial DRPs, especially their cellular role. Indeed, some bacterial DRPs have been associated with a variety of processes involving membranes *in vivo*, such as a surveillance mechanism for membrane punctures caused by antibiotics and bacteriophages (44, 45), membrane vesicle formation (46) or cytokinesis by promoting membrane curvature at the septum (47, 48). In addition, studies of the *Bacillus subtilis*

464 DRP DynA have shown that this protein can promote membrane fusion *in vitro* (49). The

465 mechanism by which the fusion operates is not yet known, but bacterial DRPs are

466 probably recruited to the sites where membrane fusion is needed (48, 50). Interestingly,

467 structural analysis of *Campylobacter jejuni* DLP1/DLP2 proteins allowed to propose a

468 mechanism explaining how these proteins attach and bind distant and opposing

469 membranes (51). Unfortunately, the cellular function of *C. jejuni* DLP1/DLP2 is currently

470 unknown. DRPs identified in this study have not yet been characterized and no

471 information on their localization and function is available. However, among the identified

472 organisms, we found, with the second-best score (E-Value 2e-80, **Table S1**), the

473 bacteria of the phylum Planctomycetes which are somewhat particular organisms.

474 Indeed, these bacteria contain a compartmentalized cytosol, separated by an

475 intracytoplasmic membrane (52), in some cases surrounding the nucleus (53) or forming

476 an anammoxosome, a pseudo-mitochondrion that is responsible for the production of

477 energy (54, 55). It is then conceivable that the identified protein in Planctomycetes

478 (*Pb*DBF, **Figure 2 and S3**) is involved in membrane structuring.

479 The role of *Tb*DBF in mitochondrial shaping was then confirmed by its

480 overexpression in PCF. Indeed, overexpressed *Tb*DBF modifies the structure of the

481 mitochondrion, with a very strong increase in connections. Moreover, the inactivation of

482 its GTPase domain (K141A mutation) also confirms its belonging to the large family of

483 dynamins. Interestingly, a similar link between hyperconnection of a branching network

484 and increased fusion processes has been reported in filamentous fungi, which grow as

485 interconnected branching networks (56). It is therefore tempting to speculate that, in

486 trypanosomes, excess *Tb*DBF increases the interconnectivity of mitochondrial networks

487 by enhanced fusion. The absence of fragmentation observed upon partial or total

488 inactivation of *Tb*DBF expression was rather expected and suggests that trypanosomes

489 differ from mammalian and yeast cells by the absence or a very low level of

490 regular/permanent mitochondrial fission. This is in agreement with previous studies

491 suggesting that fission only occurs during cell division (21, 28). It should also be kept in

492 mind that other proteins could be involved in the structuring of mitochondria as shown

493   by studies on mitochondrial outer membrane proteome in *T. brucei* (57, 58) and the

494   presence of mitochondrial complexes such as recently characterized MICOS (59). It

495   should be noted that *Tb*DBF seems to be part of a new fusion mechanism, so its

496   inactivation may not have the same effects as for Mfn or Opa1. It is also possible that

497   subtle changes in mitochondrial structure are present, but that we were not able to

498   reveal with our approaches. Another intriguing point is the absence of phenotype in

499   response to overexpression of *Tb*DBF in the BSF, which seems to reflect the relatively low

500   dynamics of the mitochondrial structuration in these parasitic forms. It is possible that

501   *Tb*DBF interacts with other partners, in a possible branching complex, that might only be

502   expressed in the PCF. However, one cannot exclude that overexpression of *Tb*DBF is not

503   high enough to initiate an increase in interconnectivity.

504   Using several microscopy approaches, we have shown that *Tb*DBF is localized in the

505   mitochondrion and more precisely in the mitochondrial membranes. *Tb*DBF contains two

506   domains involved in its accurate mitochondrial addressing, an N-terminal sequence

507   (MTS) and two C-terminal transmembrane domains. Proteins with an N-terminal MTS

508   are mainly fully imported into the mitochondrial matrix, however, some of them, such as

509   Opa1 and Apoptosis-inducing factor (AIF) face the inner membrane (60). Indeed, Opa1

510   and AIF localize mainly to the IMS due to its TM domain located in close proximity to the

511   MTS, interrupting transport across the inner membrane, which is not the case for *Tb*DBF.

512   Moreover, *Tb*DBF has a functional MTS, which is cleaved in the mitochondrial matrix and

513   its absence impacts the activity of the protein, suggesting that at least part of the protein

514   crosses OMM and IMM. However, with an MTS-less construct, the protein is still partially

515   associated to the mitochondrion and other membranes through its two C-terminal

516   transmembrane domains. It should be noted that the targeting specificity of C-terminal

517   TM domains is often determined by the amino acids flanking the TMs (61, 62) which

518   could explain the remaining *Tb*DBF protein in mitochondrion when the MTS was deleted.

519   *Tb*DBF TM domains should therefore be considered as membrane-anchoring domains.

520   Interestingly, the structure prediction of *Tb*DBF by Alphafold (63) suggests that the two

521   TM domains form a loop that may allow anchoring in the inner membrane with a possible

522 orientation of the remaining protein on the matrix side (**Figure 10**). This orientation is

523 also probably similar to the prokaryotic DBFs which could also be anchored in the plasma

524 membrane and facing the cytosol. Recently, Sheik *et al.* (22) clearly demonstrated that

525 expression of a potential DRP from giant virus in *T. brucei* PCF strongly affects

526 mitochondrial morphology within the matrix, with a close association with the inner

527 membrane. This contrasts with the mode of action of human or yeast mitofusins, which

528 are involved in the remodeling of mitochondrial outer and inner membranes, but never

529 via the matrix side. All of these results point to a complex or even unique targeting and

530 membrane topology of *Tb*DBF, different from those observed for mammalian and fungi

531 OM and IM fusion factors.

532   In many eukaryotes, mitochondria display a dynamic behaviour of constant fission

533 and fusion, with the size, appearance and organization of mitochondrial membranes

534 varying between species, tissues and physiological conditions (7). Although there is

535 considerable convincing evidence that mitochondrial dynamics and bioenergetics are

536 linked, the precise relationship between the two is still not known (6-8). It is therefore

537 tempting to assume that such tight connections regulate not only mitochondrial function

538 and energy metabolism, but also the life cycle and pathogenic potential of trypanosomes.

539 In order to identify possible metabolic variations induced by *Tb*DBF overexpression, we

540 screened 119 molecules that could be used by parasites as carbon and energy sources.

541 Only 3 molecules appeared to be more used/consumed in cells with altered mitochondria,

542 i.e., glucose, proline and ethanolamine. Glucose and proline are the two main carbon

543 sources that trypanosomes use in the mammalian host and the insect vector,

544 respectively. This suggests a greater energy demand, required either to change the

545 mitochondrial structure and/or to increase the mitochondrial content. The third molecule,

546 ethanolamine, is probably not a carbon source *per se*, but reflects a change in

547 phospholipid metabolism and more specifically in phosphatidylethanolamine (PE), which

548 together with phosphatidylcholine (PC), are the main constituents of eukaryotic cell

549 membranes. PE is preferentially distributed in the inner leaflet of mitochondrial

550 membranes and plays an essential role in mitochondrial functions (64, 65) by

551   maintaining the mitochondrial morphology (66-68). Indeed, PE is a fusogenic

552   phospholipid that confers negative curvature to the mitochondrial membrane (69) and

553   has been proposed to play important roles in membrane fusion involving the mitofusin

554   Mfn (70). In PCF *T. brucei*, PE and PC are synthesized exclusively through the Kennedy

555   pathway (71). Mutations in lipid composition result in alterations in mitochondrial

556   morphology and inhibition of respiration (72) (73). Remarkably, RNAi-mediated down-

557   regulation of ethanolamine phosphate cytidylyltransferase expression, the second

558   enzyme in the Kennedy pathway, has been shown to disrupt mitochondrial morphology

559   and ultrastructure in *T. brucei*. The most immediate effect was a change in mitochondrial

560   morphology and disruption of the inner mitochondrial membrane topology (74). Since PE

561   is   essential   for   mitochondrial   morphology,   the   increased   ethanolamine

562   utilization/consumption in *Tb*DBF-overexpressing parasites likely reflects increased

563   membrane lipid biogenesis to support the alterations in mitochondrial structure. SBF-SEM

564   analysis and 3D reconstruction of parasites expressing *Tb*DBFL showed a significant

565   increase in mitochondrial membrane biogenesis with an almost doubling of the

566   mitochondrial volume. This increased membrane biogenesis is particularly evident in the

567   vicinity of the kDNA, which is completely enveloped by a hyper-reticulated globular

568   mitochondrial structure. More work is needed to determine whether this part of the

569   mitochondrion is a preferential place for membrane biogenesis. It is therefore likely that

570   the increase in membrane biogenesis is not limited to the mitochondrial membranes, but

571   also affects the other cell membranes which may explain the significant increase of the

572   cell volume observed and thus the cellular surface. However, this increase in volume

573   does not affect the parasite's growth rate, implying that the increase in volume is

574   disconnected from mechanisms regulating cell division. More work is now required to

575   understand how *Tb*DBF induces these structural and metabolic changes, as well as its

576   mode of action.

577   In conclusion, all these results clearly revealed the presence of a novel and

578   ancestral machinery involved in mitochondrial branching in trypanosomes. In addition,

579   the wide conservation of these DRPs in many eukaryotic, bacterial and archaeal genomes

580   suggests an important role in the biology of these organisms.

MATERIALS AND METHODS

Trypanosomes and cell cultures

The PCF of *T. brucei* EATRO1125.T7T (TetR-HYG-T7RNAPOL-NEO, where TetR stands for tetracycline resistance, HYG for hygromycin, T7RNAPOL for RNA polymerase T7, and NEO for neomycin) was cultured at 27°C with 5% CO_2 in SDM79 medium containing 10% (vol/vol) heat-inactivated fetal calf serum, 5 µg/ml hemin, 25 µg/ml hygromycin and 10 µg/mL neomycin. The bloodstream form of *T. brucei* 427 90-13 (TetR-HYG-T7RNAPOL-NEO) was cultured at 37°C with 5% CO_2 in Iscove's modified Dulbecco's medium (IMDM) supplemented with 10% (vol/vol) heat-inactivated fetal calf serum (FCS), 0.2 mM β-mercaptoethanol, 36 mM $NaHCO_3$, 1 mM hypoxanthine, 0.16 mM thymidine, 1 mM sodium pyruvate, 0.05 mM bathocuproine, 1.5 mM L-cysteine (75), 5 µg/ml hygromycin and 2,5 µg/mL neomycin. Overexpression cell lines were induced with tetracycline (10 µg/mL for BSF and 1 µg/mL for PCF). Growth was monitored by daily cell counting with the cytometer Guava® Muse® and Guava® easyCyte™.

Endogenous tagging and overexpression of TbDBF

For endogenous gene tagging, primers were designed as described in (31) and PCR was performed using pPOTv7 vector as template. The pPOT used here was pPOTv7 for C-terminus 10xHA tagging (blasticidin resistance). For overexpression, DBF gene (Tb427.07.2410) was inserted in both pLew100 (phleomycine resistance) (76) and pHD1336 (blasticidin resistance) (77) expression vectors. Fragments were amplified and cloned into *Hin*dIII and *Xba*I restrictions sites of the pLew100 and into *Hin*dIII and *Bam*HI restrictions sites of the pHD1336 expression vectors. In addition, a 3xTy1 tag was added at the C-terminus of the protein in the pLew100-*Tb*DBF, using the *Xba*I and *Bam*HI restrictions sites. The truncated version of *Tb*DBF without the first 41 amino acids (*Tb*DBFΔMTS) and without the two trans-membranes domain (*Tb*DBFΔTM) were amplified and cloned in the pLew100 with a 3xTy1 tag as previously described. Catalytic mutant K141 was replaced by an alanine, using PCR approach (78) and PCR product cloned in the pLew100 with a 3xTy1 tag. EATRO1125.T7T PCF was transfected using Amaxa

610   Nucleofector®II, program X-001 and selected in SDM79 containing 25 µg/ml hygromycin

611   10 µg/mL neomycin and 5 µg/mL phleomycin. 427 90-13 BSF was transfected using the

612   same conditions and selected in IMDM containing 5 µg/ml hygromycin, 2,5 µg/mL

613   neomycin and 5 µg/mL blasticidin. Primers used for the constructions are presented in

614   supplemental **Table S2**.

615

Endogenous tagging and inactivation of TbDBF by CRISPR-Cas9

617   Endogenous tagging and inactivation of *Tb*DBF was achieved by CRISPR Cas9 technology

618   according Soares Medeiros et *al.* (35) but using *Sp*Cas9 instead of *Sa*Cas9 (more detailed

619   description of optimized and adapted protocols will be published separately). Briefly,

620   inactivation of the *Tb*DBF was achieved by inserting the resistant marker puromycin

621   (Pac) or a small sequence encoding for a *Bam*HI restriction site plus 6 successive stop

622   codons, flanked by 50 bp homologous to the 5' and 3' *Tb*DBF sequences from the Cas9

623   cutting site. Similar approaches have been performed for endogenous tagging with the

624   insertion of a sequence encoding 3xTy1 or 3xHA. The EATRO1125.T7T PCF and the 427

625   90.13 BSF (1×10^6 cells) were respectively transfected, using Amaxa nucleofectorII, with

626   1 µg of purified cassette (puromycin resistance marker, Stop*Bam*H1Stop, 3xTy1 or

627   3xHA), 30 µg Cas9 protein from IDT and pre-annealing TracrRNA (0.4 µmol) and gRNA

628   (0.4 µmol). Cells were transfected using program X-001 and selected or not with

629   puromycin (SDM79, 1 µg/mL, or IMDM 0.1 µg)/mL). Cells were cloned by using a cell

630   sorter (TBM Core facility), and selection of double inactivated *Tb*DBF gene (*Tb*DBF$^{-/-}$) or

631   endogenously tagged clones was done by DNA extraction, with NucleoSpin Blood

632   (Macherey-Nagel) and PCR amplification, see supplemental **Table S2**. Guide RNA were

633   designed using EuPaGDT, from http://tritrypdb.org. Primers and guide RNA used are

634   synthetized by Integrated DNA Technologies (IDT) and listed in supplemental **Table S2**.

635

Down-regulation of TbDBF gene expression

637   Down-regulation of DBF expression by RNAi in PCF was achieved by expression of stem-

638   loop "sense/antisense" RNA molecules targeting a 400-bp fragment of the DBF gene

introduced into the pLew100 tetracycline-inducible expression vector. A PCR-amplified 450-bp fragment, containing the antisense DBF sequence was inserted between *Xho*I and *Bam*HI restriction sites of the pLew100 plasmid. Then, the separate 400-bp PCR-amplified fragment containing the sense DBF sequence was inserted upstream of the antisense sequence, using *Hin*dIII and *Xho*I restriction sites. The resulting plasmid, pLew100-DBF-SAS, contains a sense and antisense version of the DBF fragment separated by a 50-bp fragment. The EATRO1125 PCF was transfected with the pLew100-DBF-SAS and cells were selected in SDM79 medium containing 25 µg/ml hygromycin, 10 µg/mL neomycin and 5 µg/mL phleomycin. Expression of the RNAi was induced by tetracycline (1 µg/mL).

Down-regulation of DBF expression by RNAi in BSF was achieved exactly as described (29) with a 280-bp fragment derived from the *Tb*DBF open reading frame inserted into the p2T7-177 plasmid (79). Linearized plasmid was transfected in *T. brucei* 427 90-13 (TetR-HYG-T7RNAPOL-NEO) BSF cells. Expression of the RNAi was induced by tetracycline (10 µg/mL). Primers used for the constructions are presented in supplemental **Table S2**.

Mitochondria staining on living cells

Rhodamine-123 (30 µg/mL) was added on cell culture ($5x10^6$ - $1x10^7$ cells per mL) for 15 min at room temperature, then cells were washed twice with PBS and spread on slides. Images were acquired with MetaMorph software on Axioplan 2 microscope and processed with ImageJ.

Immunofluorescence

Cells were washed twice with PBS, then fixed with 2% paraformaldehyde (PFA) for 10 min at room temperature and 0.1mM Glycine was added 10 min to stop the reaction. The cells were spread on slides and permeabilized with 0.05% triton X-100. After incubation in PBS containing 4% bovine serum albumin (BSA) 20 min, cells were incubated for 1 hour with primary antibodies diluted in PBS-BSA 4%, washed 4 times with PBS and

668   incubated for 45 min with secondary antibodies diluted in PBS-BSA 4% followed by three

669   washes. Then, kinetoplasts and nuclei were labelled with DAPI (10 μg/mL) for 5 min.

670   Slides were washed 3 times with PBS and mounted with SlowFade Gold (Molecular

671   probes). Images were acquired with MetaMorph software on Zeiss Imager Z1 or Axioplan

672   2 microscope and processed with ImageJ.

673

674   ***Ultrastructure Expansion Microscopy (UExM)***

675   The protocol of UExM realized exactly as described by Casas et *al.* 2022

676   (dx.doi.org/10.17504/protocols.io.bvwqn7dw). An expansion factor was determined

677   using the ratio between the size of the coverslip (12mm) and the size of the gels after

678   the first expansion. Images were acquired on a confocal Leica SP5-MP (Bordeaux

679   Imaging Center) using a 63X oil objective and processed with ImageJ.

680

681   ***Immunoelectron microscopy***

682   Harvested cells were placed on the surface of formvar-coated copper grids (400 mesh).

683   Each loop was quickly submersed in liquid propane ($-180°C$) and transferred into a

684   precooled solution of 0.1% uranyl acetate in dry acetone for 3 days at -82°C. Samples

685   were rinsed with acetone at -20°C, and embedded progressively at -20°C in LR Gold

686   resin (EMS, USA). Resin polymerization was carried out at -20°C for 7 days under UV

687   illumination. Ultrathin LR Gold sections were collected on nickel grids coated with

688   formvar. Sections were first incubated for 15 min with NH_4Cl 500mM in Tris-buffered

689   saline (TBS) pH7.8, blocked 2x10 min with 2% BSA in TBS pH 7.8. The grids were

690   incubated 1 hour at room temperature with anti Ty1 antibody diluted to 1:200 in TBS

691   containing 2% BSA rinsed with TBS containing 2% BSA and with TBS containing 1% BSA.

692   The samples were then incubated for 1 hour at room temperature with anti-mouse IgG

693   diluted to 1:20 conjugated to 10 nm gold particles (BioCell). The sections were rinsed

694   with TBS containing 1% BSA, and fix with 1% glutaraldehyde in TBS. After rinsing with

695   TBS, grids were contrasted through a 5 min incubation with 2% uranyl acetate in water,

696   followed by 1 min incubation with 1% lead citrate. Observations were performed on a

697   HITACHI 7650 electron microscope operated at 80 KV with a Gatan-11 MPx camera (PIE

698   Bordeaux Imaging Center).

699

700   ***SBF-SEM***

701   Cells were prepared as described by Blancard and Salin (80) except for freeze-

702   substitution medium (0.1% potassium permanganate for 24 h followed by 0.1% tannic

703   acid for 24 h, and 2% osmium tetroxide with 1% uranyl acetate for 3 days). Resin-

704   embedded samples were trimmed, mounted onto stubs and placed into a Zeiss

705   GeminiSEM300 with a fitted Gatan 3View2XP system (Gatan, Abingdon, UK). Serial

706   images of the block face were recorded at an accelerating voltage of 1.2 kV. All images

707   were taken with the following scanning settings: Pixel size 10 nm, pixel time 5 µs, slice

708   thickness 50 nm (Z-slice), image size 5000x5000. Between 700 and 900 images were

709   collected for each run. Images were collected from Back scattered electron with a specific

710   BSE Detector (On point - Gatan Inc., Pleasanton, CA, USA) using the software Digital

711   Micrograph (Gatan). Images were combined to form a single stack. Data processing and

712   statistical analysis: Segmentation was conducted using AMIRA (versions 5.2.0

713   Thermofisher Scientific). Manual segmentation of cells and organelles were conducted

714   using the brush tool and was based on ultrastructural characteristics specific to each

715   organelle. Each organelle was segmented using the organelle membrane as the outer

716   edge. Surface models were produced for each segmented organelle. Volumes of

717   organelles were automatically generated from the surface renderings of segmented data.

718

719   ***Western-blot***

720   Total protein extracts ($5x10^6$ cells) were separated by SDS-PAGE (10%) and

721   immunoblotted on TransBlot Turbo Midi-size PVDF Membranes (Bio-Rad).

722   Immunodetection was performed using the primary antibodies, diluted in PBS-Tween-

723   Milk (0.05% Tween20, 5% skimmed milk powder), summarized in supplemental **Table**

724   **S3**. Revelation was performed using a second antibody coupled to the HRP and the

725   Clarity Western enhanced-chemiluminescence (ECL) substrate as describes by the

726 manufacturer (Bio-Rad). Images were acquired and analyzed with the ImageQuant Las

727 4000 luminescent image analyzer.

728

729 ***Biolog***

730 Biolog Phenotype MicroArrays™ provide an easy-to-use technology for scanning and

731 measuring the energy metabolism pathways present in a wide range of *in vitro* cultured

732 cell types. The metabolic pathway activities are assayed with a simple colorimetric

733 reagent that measures redox energy produced when a cell oxidizes a chemical

734 (Tetrazolium reduction). Standard protocol described by the manufacturer (Biolog) has

735 been used with the following modifications: cells were resuspended in Biolog IF-M1 buffer

736 at $1x10^7$ cells per mL and 50 µL of this cell suspension were pre-incubated in each well of

737 the PM-M1 or PM-M2 plates for 1 hours at 27°C with 5% CO_2. Then, 10 µL of Biolog Dye

738 Mix (Mix MB) was added to all plate wells and load into the Omnilog® for kinetic reading

739 for 18 hours at 27°C or endpoint measurement at 590 nm with a microplate reader after

740 18 hours.

741

742 ***Quantification of Mitochondrial junctions - ImageJ macro***

743 To quantify number of mitochondrial junctions, an ImageJ macro was developed with the

744 help of the Bordeaux Imaging Center (BIC). The script is presented in supplemental

745 Materials and Methods data **MMS1**.

746

747 ***Statistical analysis***

748 Experiments were performed at least in triplicates. Statistical analyses were performed

749 using Prism (GraphPad) software. The results are presented as mean ± S.D. Where

750 indicated the results were subjected to two-sided student's t-test to determine statistical

751 differences against the indicated group (Confidence interval 95% - P-value style: 0.1234

752 (ns); 0.0332 (*); 0.0021 (**); 0.0002 (***); <0.0001 (****)).

753

754 ***Structural prediction software and sequence analysis***

755   Structure   predictions   were   performed   using   PSIPRED
756   ("http://bioinf.cs.ucl.ac.uk/psipred/") (81) and prediction of mitochondrial targeting
757   sequences by various algorythms (MitoprotII, MitoFates and iPSORT) (82). Phylogeny
758   analysis was performed with Geneious software using default parameters and the
759   neighbor-joining method was used for tree calculation.

REFERENCES

769

770 1.   Bohringer S, Hecker H. Quantitative ultrastructural investigations of the life cycle
771 of Trypanosoma brucei: a morphometric analysis. J Protozool. 1975;22(4):463-7.

772 2.   Priest JW, Hajduk SL. Developmental regulation of Trypanosoma brucei
773 cytochrome c reductase during bloodstream to procyclic differentiation. Mol Biochem
774 Parasitol. 1994;65(2):291-304.

775 3.   van Hellemond JJ, Opperdoes FR, Tielens AG. The extraordinary mitochondrion
776 and unusual citric acid cycle in Trypanosoma brucei. Biochem Soc Trans. 2005;33(Pt
777 5):967-71.

778 4.   Michels PA, Bringaud F, Herman M, Hannaert V. Metabolic functions of glycosomes
779 in trypanosomatids. Biochim Biophys Acta. 2006;1763(12):1463-77.

780 5.   Matthews KR. The developmental cell biology of Trypanosoma brucei. J Cell Sci.
781 2005;118(Pt 2):283-90.

782 6.   Duvezin-Caubet S, Jagasia R, Wagener J, Hofmann S, Trifunovic A, Hansson A, et
783 al. Proteolytic processing of OPA1 links mitochondrial dysfunction to alterations in
784 mitochondrial morphology. J Biol Chem. 2006;281(49):37972-9.

785 7.   Sauvanet C, Duvezin-Caubet S, di Rago JP, Rojo M. Energetic requirements and
786 bioenergetic modulation of mitochondrial morphology and dynamics. Semin Cell Dev Biol.
787 2010;21(6):558-65.

788 8.   Silva Ramos E, Larsson NG, Mourier A. Bioenergetic roles of mitochondrial fusion.
789 Biochim Biophys Acta. 2016;1857(8):1277-83.

790 9.   Chan DC. Fusion and fission: interlinked processes critical for mitochondrial
791 health. Annual review of genetics. 2012;46:265-87.

792 10.   Westermann B. Mitochondrial fusion and fission in cell life and death. Nat Rev Mol
793 Cell Biol. 2010;11(12):872-84.

794 11.   Sesaki H, Adachi Y, Kageyama Y, Itoh K, Iijima M. In vivo functions of Drp1:
795 lessons learned from yeast genetics and mouse knockouts. Biochim Biophys Acta.
796 2014;1842(8):1179-85.

797 12.   Otera H, Ishihara N, Mihara K. New insights into the function and regulation of
798 mitochondrial fission. Biochim Biophys Acta. 2013;1833(5):1256-68.

799   13.   Malka F, Guillery O, Cifuentes-Diaz C, Guillou E, Belenguer P, Lombes A, et al.
800   Separate fusion of outer and inner mitochondrial membranes. EMBO Rep.
801   2005;6(9):853-9.

802   14.   Song Z, Ghochani M, McCaffery JM, Frey TG, Chan DC. Mitofusins and OPA1
803   mediate sequential steps in mitochondrial membrane fusion. Mol Biol Cell.
804   2009;20(15):3525-32.

805   15.   Legros F, Lombes A, Frachon P, Rojo M. Mitochondrial fusion in human cells is
806   efficient, requires the inner membrane potential, and is mediated by mitofusins. Mol Biol
807   Cell. 2002;13(12):4343-54.

808   16.   Bertholet AM, Delerue T, Millet AM, Moulis MF, David C, Daloyau M, et al.
809   Mitochondrial fusion/fission dynamics in neurodegeneration and neuronal plasticity.
810   Neurobiol Dis. 2016;90:3-19.

811   17.   Jakob M, Hoffmann A, Amodeo S, Peitsch C, Zuber B, Ochsenreiter T.
812   Mitochondrial growth during the cell cycle of Trypanosoma brucei bloodstream forms. Sci
813   Rep. 2016;6:36565.

814   18.   Hughes L, Borrett S, Towers K, Starborg T, Vaughan S. Patterns of organelle
815   ontogeny through a cell cycle revealed by whole-cell reconstructions using 3D electron
816   microscopy. J Cell Sci. 2017;130(3):637-47.

817   19.   Gibson W, Crow M, Kearns J. Kinetoplast DNA minicircles are inherited from both
818   parents in genetic crosses of Trypanosoma brucei. Parasitol Res. 1997;83(5):483-8.

819   20.   Esseiva AC, Chanez AL, Bochud-Allemann N, Martinou JC, Hemphill A, Schneider
820   A. Temporal dissection of Bax-induced events leading to fission of the single
821   mitochondrion in Trypanosoma brucei. EMBO Rep. 2004;5(3):268-73.

822   21.   Chanez AL, Hehl AB, Engstler M, Schneider A. Ablation of the single dynamin of T.
823   brucei blocks mitochondrial fission and endocytosis and leads to a precise cytokinesis
824   arrest. J Cell Sci. 2006;119(Pt 14):2968-74.

825   22.   Sheikh S, Panek T, Gahura O, Tyc J, Zahonova K, Lukes J, et al. A Novel Group of
826   Dynamin-Related Proteins Shared by Eukaryotes and Giant Viruses Is Able to Remodel
827   Mitochondria From Within the Matrix. Mol Biol Evol. 2023;40(6).

828   23.   Sesaki H, Jensen RE. Division versus fusion: Dnm1p and Fzo1p antagonistically
829   regulate mitochondrial shape. J Cell Biol. 1999;147(4):699-706.

830   24.   Bleazard W, McCaffery JM, King EJ, Bale S, Mozdy A, Tieu Q, et al. The dynamin-
831   related GTPase Dnm1 regulates mitochondrial fission in yeast. Nature cell biology.
832   1999;1(5):298-304.

833   25.   DiMaio J, Ruthel G, Cannon JJ, Malfara MF, Povelones ML. The single
834   mitochondrion of the kinetoplastid parasite Crithidia fasciculata is a dynamic network.
835   PLoS ONE. 2018;13(12):e0202711.

836   26.   Logan DC. Plant mitochondrial dynamics. Biochim Biophys Acta. 2006;1763(5-
837   6):430-41.

838   27.   Arimura SI. Fission and Fusion of Plant Mitochondria, and Genome Maintenance.
839   Plant Physiol. 2018;176(1):152-61.

840   28.   Morgan GW, Goulding D, Field MC. The single dynamin-like protein of
841   Trypanosoma brucei regulates mitochondrial division and is not required for endocytosis.
842   J Biol Chem. 2004;279(11):10692-701.

843   29.   Vanwalleghem G, Fontaine F, Lecordier L, Tebabi P, Klewe K, Nolan DP, et al.
844   Coupling of lysosomal and mitochondrial membrane permeabilization in trypanolysis by
845   APOL1. Nature communications. 2015;6:8078.

846   30.   Dean S, Sunter JD, Wheeler RJ. TrypTag.org: A Trypanosome Genome-wide
847   Protein Localisation Resource. Trends Parasitol. 2017;33(2):80-2.

848   31.   Dean S, Sunter J, Wheeler RJ, Hodkinson I, Gluenz E, Gull K. A toolkit enabling
849   efficient, scalable and reproducible gene tagging in trypanosomatids. Open Biol.
850   2015;5(1):140197.

851   32.   Urbaniak MD, Guther ML, Ferguson MA. Comparative SILAC proteomic analysis of
852   Trypanosoma brucei bloodstream and procyclic lifecycle stages. PLoS ONE.
853   2012;7(5):e36619.

854   33.   Millerioux Y, Ebikeme C, Biran M, Morand P, Bouyssou G, Vincent IM, et al. The
855   threonine degradation pathway of the Trypanosoma brucei procyclic form: the main
856   carbon source for lipid biosynthesis is under metabolic control. Mol Microbiol.
857   2013;90(1):114-29.

858   34.   Nunnari J, Marshall WF, Straight A, Murray A, Sedat JW, Walter P. Mitochondrial
859   transmission during mating in Saccharomyces cerevisiae is determined by mitochondrial
860   fusion and fission and the intramitochondrial segregation of mitochondrial DNA. Mol Biol
861   Cell. 1997;8(7):1233-42.

862   35.   Soares Medeiros LC, South L, Peng D, Bustamante JM, Wang W, Bunkofske M, et
863   al. Rapid, Selection-Free, High-Efficiency Genome Editing in Protozoan Parasites Using
864   CRISPR-Cas9 Ribonucleoproteins. MBio. 2017;8(6).

865   36.   Hales KG, Fuller MT. Developmentally regulated mitochondrial fusion mediated by
866   a conserved, novel, predicted GTPase. Cell. 1997;90(1):121-9.

867   37.   Hermann GJ, Thatcher JW, Mills JP, Hales KG, Fuller MT, Nunnari J, et al.
868   Mitochondrial fusion in yeast requires the transmembrane GTPase Fzo1p. J Cell Biol.
869   1998;143(2):359-73.

870   38.   Santel A, Frank S, Gaume B, Herrler M, Youle RJ, Fuller MT. Mitofusin-1 protein is
871   a generally expressed mediator of mitochondrial fusion in mammalian cells. J Cell Sci.
872   2003;116(Pt 13):2763-74.

873   39.   Gambarotto D, Hamel V, Guichard P. Ultrastructure expansion microscopy (U-
874   ExM). Methods in cell biology. 2021;161:57-81.

875   40.   Amodeo S, Kalichava A, Fradera-Sola A, Bertiaux-Lequoy E, Guichard P, Butter F,
876   et al. Characterization of the novel mitochondrial genome segregation factor TAP110 in
877   Trypanosoma brucei. J Cell Sci. 2021;134(5).

878   41.   Richmond GS, Gibellini F, Young SA, Major L, Denton H, Lilley A, et al. Lipidomic
879   analysis of bloodstream and procyclic form Trypanosoma brucei. Parasitology.
880   2010;137(9):1357-92.

881   42.   Daumke O, Praefcke GJ. Invited review: Mechanisms of GTP hydrolysis and
882   conformational transitions in the dynamin superfamily. Biopolymers. 2016;105(8):580-
883   93.

884   43.   Ramachandran R, Schmid SL. The dynamin superfamily. Curr Biol.
885   2018;28(8):R411-R6.

886   44.   Sawant P, Eissenberger K, Karier L, Mascher T, Bramkamp M. A dynamin-like
887   protein involved in bacterial cell membrane surveillance under environmental stress.
888   Environ Microbiol. 2016;18(8):2705-20.

889   45.   de Sousa Borges A, Scheffers DJ. Bacterial dynamin as a membrane puncture
890   repair kit. Environ Microbiol. 2016;18(8):2298-301.

891   46.   Michie KA, Boysen A, Low HH, Moller-Jensen J, Lowe J. LeoA, B and C from
892   enterotoxigenic Escherichia coli (ETEC) are bacterial dynamins. PLoS ONE.
893   2014;9(9):e107211.

894   47.   Schlimpert S, Wasserstrom S, Chandra G, Bibb MJ, Findlay KC, Flardh K, et al.
895   Two dynamin-like proteins stabilize FtsZ rings during Streptomyces sporulation. Proc Natl
896   Acad Sci U S A. 2017;114(30):E6176-E83.

897   48.   Bramkamp M. Structure and function of bacterial dynamin-like proteins. Biol
898   Chem. 2012;393(11):1203-14.

899   49.   Burmann F, Ebert N, van Baarle S, Bramkamp M. A bacterial dynamin-like protein
900   mediating nucleotide-independent membrane fusion. Mol Microbiol. 2011;79(5):1294-
901   304.

902   50.   Jimah JR, Hinshaw JE. Structural Insights into the Mechanism of Dynamin
903   Superfamily Proteins. Trends Cell Biol. 2019;29(3):257-73.

904   51.   Liu J, Noel JK, Low HH. Structural basis for membrane tethering by a bacterial
905   dynamin-like pair. Nature communications. 2018;9(1):3345.

906   52.   Lindsay MR, Webb RI, Fuerst JA. Pirellulosomes: a new type of membrane-
907   bounded cell compartment in planctomycete bacteria of the genus Pirellula. Microbiology
908   (Reading). 1997;143(3):739-48.

909   53.   Fuerst JA, Webb RI. Membrane-bounded nucleoid in the eubacterium Gemmata
910   obscuriglobus. Proc Natl Acad Sci U S A. 1991;88(18):8184-8.

911   54.   Jogler C. The bacterial 'mitochondrium'. Mol Microbiol. 2014;94(4):751-5.

912   55.   Neumann S, Wessels HJ, Rijpstra WI, Sinninghe Damste JS, Kartal B, Jetten MS,
913   et al. Isolation and characterization of a prokaryotic cell organelle from the anammox
914   bacterium Kuenenia stuttgartiensis. Mol Microbiol. 2014;94(4):794-802.

915   56.   Herzog S, Schumann MR, Fleissner A. Cell fusion in Neurospora crassa. Current
916   opinion in microbiology. 2015;28:53-9.

917   57.   Niemann M, Wiese S, Mani J, Chanfon A, Jackson C, Meisinger C, et al.
918   Mitochondrial outer membrane proteome of Trypanosoma brucei reveals novel factors
919   required to maintain mitochondrial morphology. Mol Cell Proteomics. 2013;12(2):515-28.

920   58.   Povelones ML, Tiengwe C, Gluenz E, Gull K, Englund PT, Jensen RE. Mitochondrial
921   shape and function in trypanosomes requires the outer membrane protein, TbLOK1. Mol
922   Microbiol. 2013;87(4):713-29.

923   59.   Kaurov I, Vancova M, Schimanski B, Cadena LR, Heller J, Bily T, et al. The
924   Diverged Trypanosome MICOS Complex as a Hub for Mitochondrial Cristae Shaping and
925   Protein Import. Curr Biol. 2018;28(21):3393-407 e5.

926 60. Otera H, Ohsakaya S, Nagaura Z, Ishihara N, Mihara K. Export of mitochondrial
927 AIF in response to proapoptotic stimuli depends on processing at the intermembrane
928 space. EMBO J. 2005;24(7):1375-86.

929 61. Costello JL, Castro IG, Camoes F, Schrader TA, McNeall D, Yang J, et al. Predicting
930 the targeting of tail-anchored proteins to subcellular compartments in mammalian cells. J
931 Cell Sci. 2017;130(9):1675-87.

932 62. Huang X, Zhou X, Hu X, Joshi AS, Guo X, Zhu Y, et al. Sequences flanking the
933 transmembrane segments facilitate mitochondrial localization and membrane fusion by
934 mitofusin. Proc Natl Acad Sci U S A. 2017;114(46):E9863-E72.

935 63. Jumper J, Evans R, Pritzel A, Green T, Figurnov M, Ronneberger O, et al. Highly
936 accurate protein structure prediction with AlphaFold. Nature. 2021;596(7873):583-9.

937 64. Gonzalvez F, Gottlieb E. Cardiolipin: setting the beat of apoptosis. Apoptosis.
938 2007;12(5):877-85.

939 65. Ardail D, Privat JP, Egret-Charlier M, Levrat C, Lerme F, Louisot P. Mitochondrial
940 contact sites. Lipid composition and dynamics. J Biol Chem. 1990;265(31):18797-802.

941 66. Tamura Y, Endo T, Iijima M, Sesaki H. Ups1p and Ups2p antagonistically regulate
942 cardiolipin metabolism in mitochondria. J Cell Biol. 2009;185(6):1029-45.

943 67. Osman C, Haag M, Potting C, Rodenfels J, Dip PV, Wieland FT, et al. The genetic
944 interactome of prohibitins: coordinated control of cardiolipin and
945 phosphatidylethanolamine by conserved regulators in mitochondria. J Cell Biol.
946 2009;184(4):583-96.

947 68. Kuroda T, Tani M, Moriguchi A, Tokunaga S, Higuchi T, Kitada S, et al. FMP30 is
948 required for the maintenance of a normal cardiolipin level and mitochondrial morphology
949 in the absence of mitochondrial phosphatidylethanolamine synthesis. Mol Microbiol.
950 2011;80(1):248-65.

951 69. van den Brink-van der Laan E, Killian JA, de Kruijff B. Nonbilayer lipids affect
952 peripheral and integral membrane proteins via changes in the lateral pressure profile.
953 Biochim Biophys Acta. 2004;1666(1-2):275-88.

954 70. Joshi AS, Thompson MN, Fei N, Huttemann M, Greenberg ML. Cardiolipin and
955 mitochondrial phosphatidylethanolamine have overlapping functions in mitochondrial
956 fusion in Saccharomyces cerevisiae. J Biol Chem. 2012;287(21):17589-97.

957   71.   Signorell A, Rauch M, Jelk J, Ferguson MA, Butikofer P. Phosphatidylethanolamine
958   in Trypanosoma brucei is organized in two separate pools and is synthesized exclusively
959   by the Kennedy pathway. J Biol Chem. 2008;283(35):23636-44.

960   72.   Guler JL, Kriegova E, Smith TK, Lukes J, Englund PT. Mitochondrial fatty acid
961   synthesis is required for normal mitochondrial morphology and function in Trypanosoma
962   brucei. Mol Microbiol. 2008;67(5):1125-42.

963   73.   Fridberg A, Olson CL, Nakayasu ES, Tyler KM, Almeida IC, Engman DM.
964   Sphingolipid synthesis is necessary for kinetoplast segregation and cytokinesis in
965   Trypanosoma brucei. J Cell Sci. 2008;121(Pt 4):522-35.

966   74.   Signorell A, Gluenz E, Rettig J, Schneider A, Shaw MK, Gull K, et al. Perturbation
967   of phosphatidylethanolamine synthesis affects mitochondrial morphology and cell-cycle
968   progression in procyclic-form Trypanosoma brucei. Mol Microbiol. 2009;72(4):1068-79.

969   75.   Hirumi H, Hirumi K. Continuous cultivation of Trypanosoma brucei blood stream
970   forms in a medium containing a low concentration of serum protein without feeder cell
971   layers. J Parasitol. 1989;75(6):985-9.

972   76.   Wirtz E, Leal S, Ochatt C, Cross GA. A tightly regulated inducible expression
973   system for conditional gene knock-outs and dominant-negative genetics in Trypanosoma
974   brucei. Mol Biochem Parasitol. 1999;99(1):89-101.

975   77.   Biebinger S, Wirtz LE, Lorenz P, Clayton C. Vectors for inducible expression of
976   toxic gene products in bloodstream and procyclic Trypanosoma brucei. Mol Biochem
977   Parasitol. 1997;85(1):99-112.

978   78.   Ling MM, Robinson BH. Approaches to DNA mutagenesis: an overview. Anal
979   Biochem. 1997;254(2):157-78.

980   79.   Wickstead B, Ersfeld K, Gull K. Targeting of a tetracycline-inducible expression
981   system to the transcriptionally silent minichromosomes of Trypanosoma brucei. Mol
982   Biochem Parasitol. 2002;125(1-2):211-6.

983   80.   Blancard C, Salin B. Plunge Freezing: A Tool for the Ultrastructural and
984   Immunolocalization Studies of Suspension Cells in Transmission Electron Microscopy. J
985   Vis Exp. 2017(123).

986   81.   Jones DT. Protein secondary structure prediction based on position-specific scoring
987   matrices. J Mol Biol. 1999;292(2):195-202.

988   82.   Claros MG, Vincens P. Computational method to predict mitochondrially imported
989   proteins and their targeting sequences. Eur J Biochem. 1996;241(3):779-86.

990   83.   Hannaert V, Albert MA, Rigden DJ, da Silva Giotto MT, Thiemann O, Garratt RC,

991   Van Roy J, Opperdoes FR, Michels PAM. Kinetic characterization, structure modelling

992   studies and crystallization of Trypanosoma brucei enolase. Eur J Biochem.

993   2003;270:3205-13.
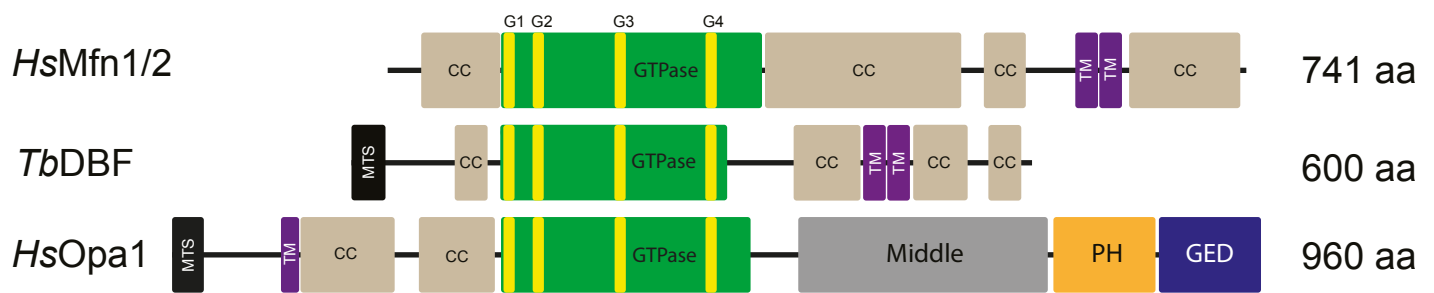
994

Figure 1 - Structure comparison between mitochondrial dynamin-related proteins (DRPs): Human mitofusin 1 or 2 (*Hs*Mfn1/2), *T. brucei Tb*DBF, and human Opa1 (*Hs*Opa1). MTS, predicted mitochondrial targeting sequence; CC, coiled-coil region; green box, GTPase domain with the four GTP-binding motifs in yellow; TM, transmembrane span; Middle, dynamin middle domain; PH, pleckstrin homology domain; GED, GTPase effector domain. Structure predictions were performed using PSIPRED (Jones, 1999). More details and sequences alignment are shown in Figure S1.
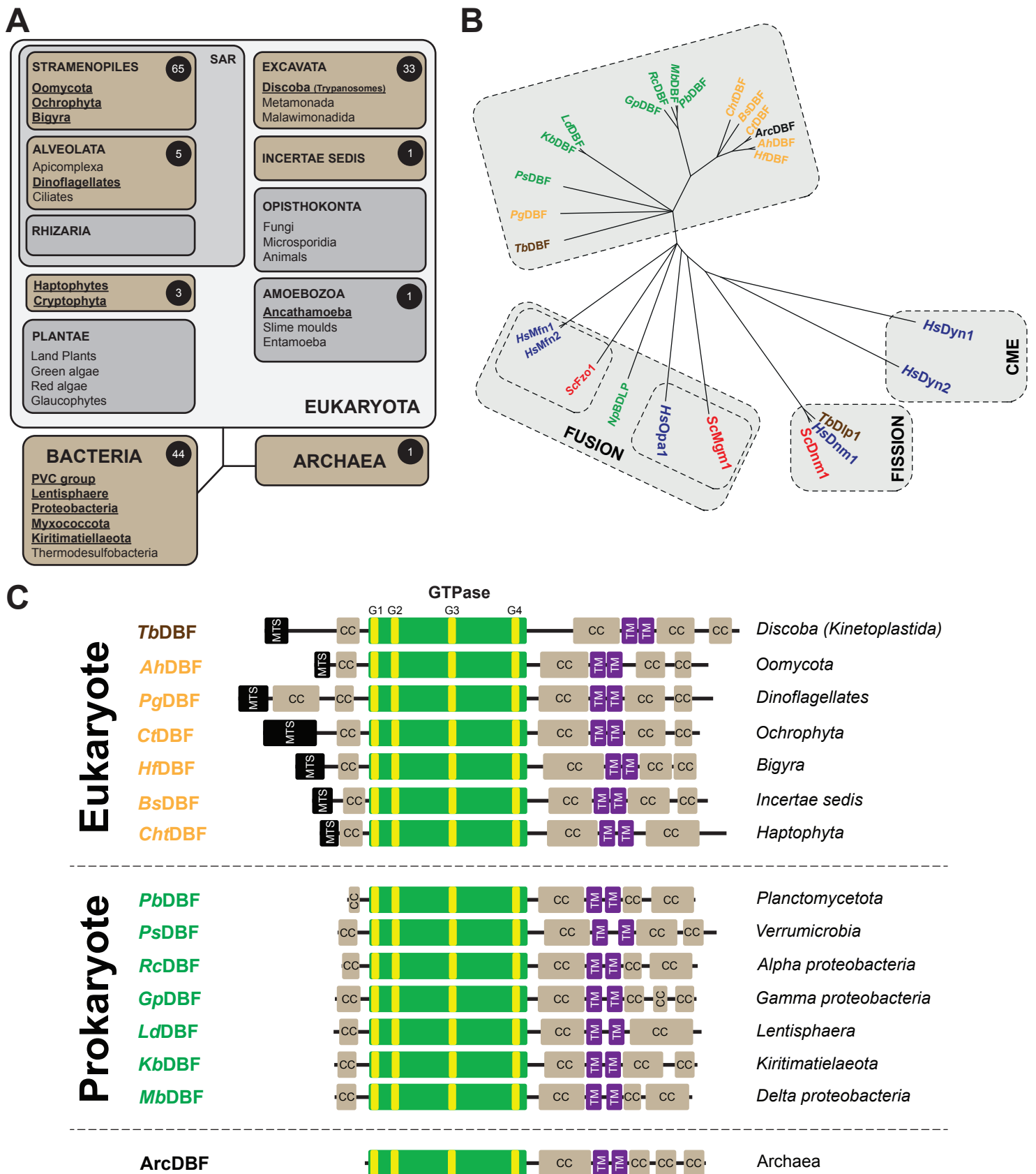
Figure 2 – Homologous sequences to *Tb*DBF, phylogenetic analysis and domain organization of the proteins. (A) Schematic view of the results of the database analysis. The black circles indicate the number of different organisms identified. Bold and underlined characters indicate taxon where homologous sequences were identified. **(B)** Phylogeny of the homologous *Tb*DBF sequences. Trypanosome sequences are highlighted in brown, mammals in blue, yeast in red, other eukaryotes in orange, prokaryote in green and Archaea in black. Mammal, yeast and trypanosome mitochondrial fission and fusion factors were also included as well as the mammals Clathrin-mediated endocytosis dynamins (CME, *Hs*Dyn1 and *Hs*Dyn2). Phylogeny analysis was performed using Geneious software with default parameters (unrooted and scaled). **(C)** Domain organization of several identified proteins from various organisms. MTS, predicted mitochondrial targeting sequence; CC, coiled-coil region; green box, GTPase domain with the four GTP-binding motifs in yellow; TM, transmembrane span; Structure predictions were performed using PSIPRED. More details and sequences alignment are shown in Figure S3. *Tb*DBF, *Trypanosoma brucei* DBF (ID: Tb927.7.2410); *Ah*DBF, *Achlya hypogyna* (ID: OQR970001); *Pg*DBF, *Polarella glacialis* (ID: CAE8737761.1); *Ct*DBF, *Chaetoceros tenuissimus* (ID: GFH50037.1); *Hf*DBF, *Hondaea fermentalgiana* (ID: GBG23909.1); *Bs*DBF, *Bactrachochytrium salamandrivorans* (ID: KAH9255760.1); *Cht*DBF, *Chrysochromulina tobinii* (ID: KOO35358.1); *Pb*DBF, *Planctomycetaceae bacterium* (ID: MBV8881356.1); *Ps*DBF, *Pedosphaera sp.* (ID: MCH2381658.1); *Rc*DBF, *Rubrimonas cliftonensis* (ID: WP_093253540.1); *Gp*DBF, *Gammaproteobacteria bacterium* (ID: RTZ59088.1); *Ld*DBF, *Lentisphaerae bacterium* (ID: NLB69313.1); *Kb*DBF, *Kiritimatiellae bacterium* (MBO7223041.1); *Mb*DBF, *Myxococcota bacterium* (MBU0550280.1). *Arc*DBF, *Archaeon* (ID: RYH26728.1); *Tb*Dlp1, *Trypanosoma brucei* Dlp1 (ID: Tb927.3.4720); *Hs*Dnm1, *Homo sapiens* Dnm1 (ID: AAH50279); *Sc*Dnm1, *Saccharomyces cerevisiae* Dnm1 (ID: AJV55509); *Hs*Dyn1 and *Hs*Dyn2, *homo sapiens* Clathrin-mediated endocytosis dynamins 1 and 2 (ID: KAI2554107.1 and ID: NP_001005360 respectively); *Hs*Opa1, *Homo sapiens* Opa1 (ID: NP_056375); *Sc*Mgm1, *Saccharomyces cerevisiae* Mgm1 (ID: NP_014854); *Np*BDLP, *Nostoc punctiforme* (ID: WP_012412711); *Hs*Mfn1 and *Hs*Mfn2, *Homo sapiens* Mfn1 and 2 (ID: NP_284941 and ID: NP_001121132 respectively); *Sc*Fzo1, *Saccharomyces cerevisiae* Fzo1 (ID: NP_009738).
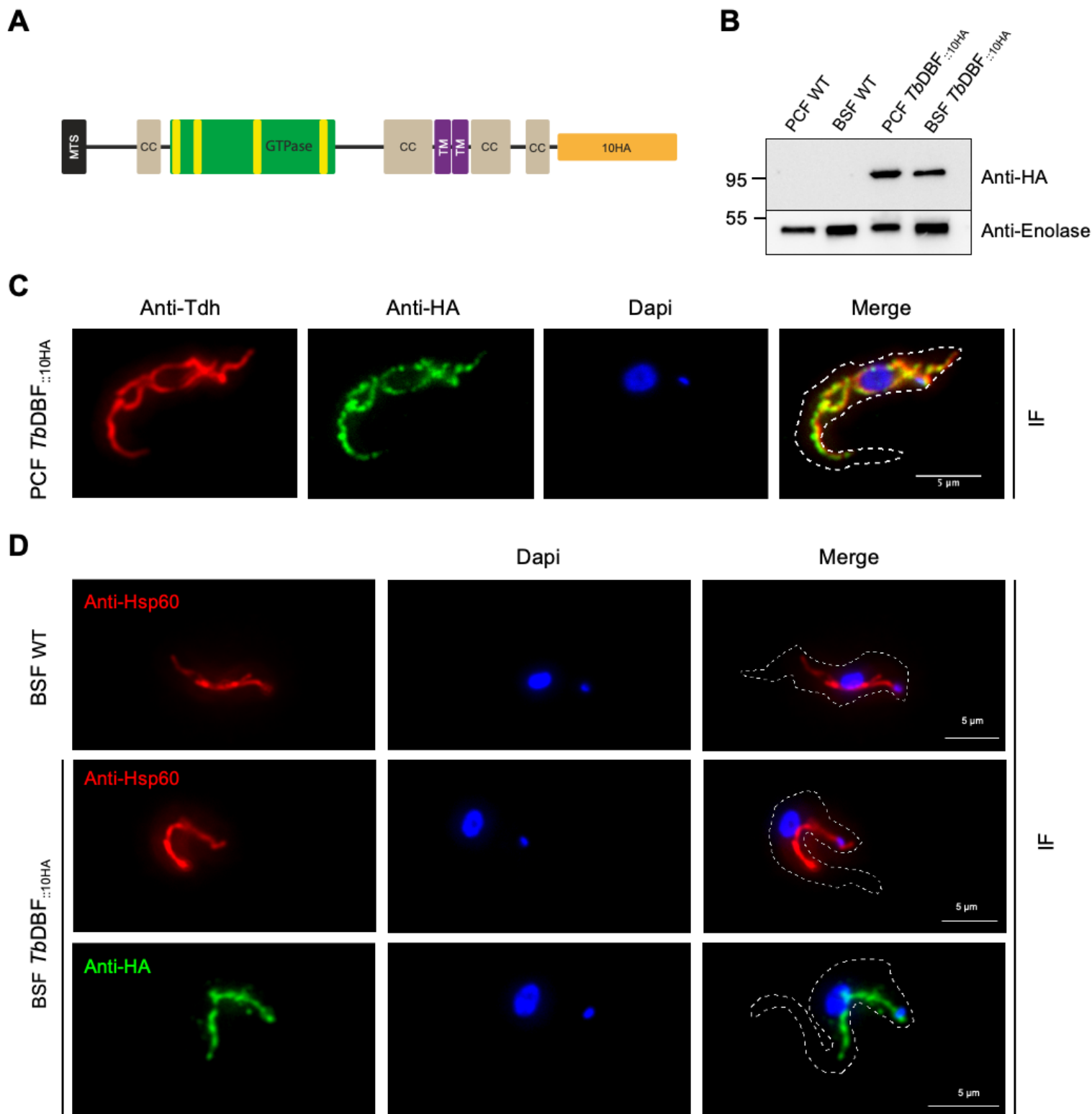
Figure 3 - Subcellular localization of *Tb*DBF. (A) Schematic representation of *Tb*DBF endogenously tagged its at C-terminus extremity with 10xHA. Only one of the two alleles is tagged. **(B)** Western blotting of whole-cell extracts (5×10^6 cells) of *T. brucei* PCF or BSF wild-type cells and PCF or BSF expressing *Tb*DBF$_{::10HA}$ cells revealed with an anti-HA antibody. It should be noted that Enolase used as a loading control is about 3 to 4 times more expressed in BSF than PCF according to Hannaert *et al.* (82). **(C)** Subcellular localization of *Tb*DBF$_{::10HA}$ in PCF. Colocalization of *Tb*DBF$_{::10HA}$ (anti-HA antibody) with matrix mitochondrial threonine dehydrogenase (Anti-Tdh antibody) analyzed by standard immunofluorescence. **(D)** Subcellular localization of *Tb*DBF$_{::10HA}$ in BSF. Matrix mitochondrial Heat shock protein 60 (Anti-Hsp60 antibody) was used to labelled the mitochondrial compartment in wild-type and *Tb*DBF$_{::10HA}$ cells.
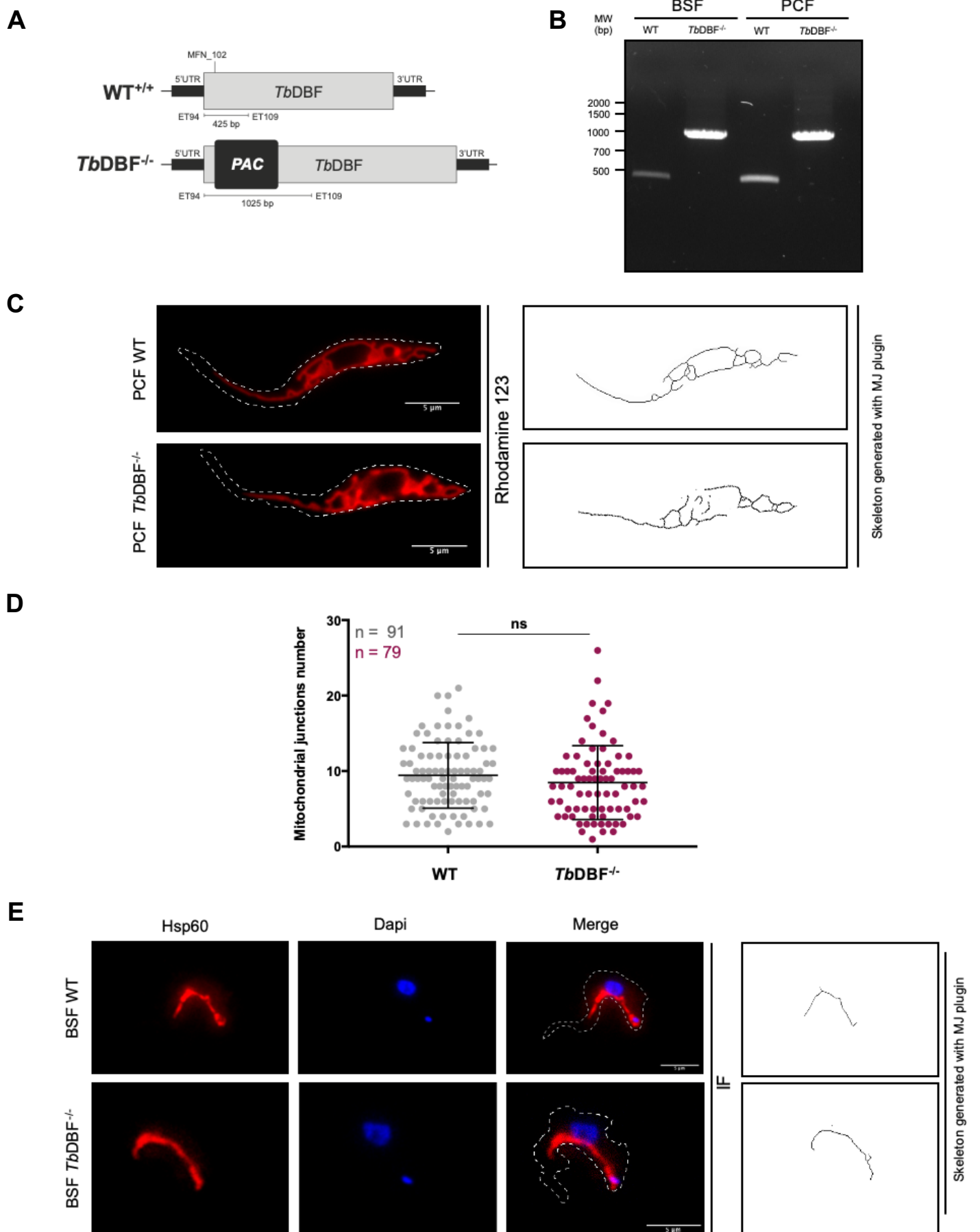
Figure 4 - Inactivation of the *Tb*DBF gene. (A) Schematic representation of *Tb*DBF inactivation by insertion of the puromycine resistant marker (PAC). **(B)** PCR confirmation of *Tb*DBF gene inactivation on both alleles in BSF and PCF. **(C)** The mitochondrial shape of living WT and *Tb*DBF⁻/⁻ PCF cells (right panel) was designed by an ImageJ macro (MJ, Mitochondrial Junctions) from rhodamine 123 staining (left panel). **(D)** Corresponding mitochondrial junctions quantification. **(E)** Antibody directed against Hsp60 was used to label and visualized mitochondrial shape in BSF cells. Top panel : BSF WT cell; bottom panel : BSF *Tb*DBF⁻/⁻ cell. Statistic : t test - Confidence interval 95% - P-value style : 0.1234 (ns); 0.0332 (*); 0.0021 (**); 0.0002 (***); <0.0001 (****).
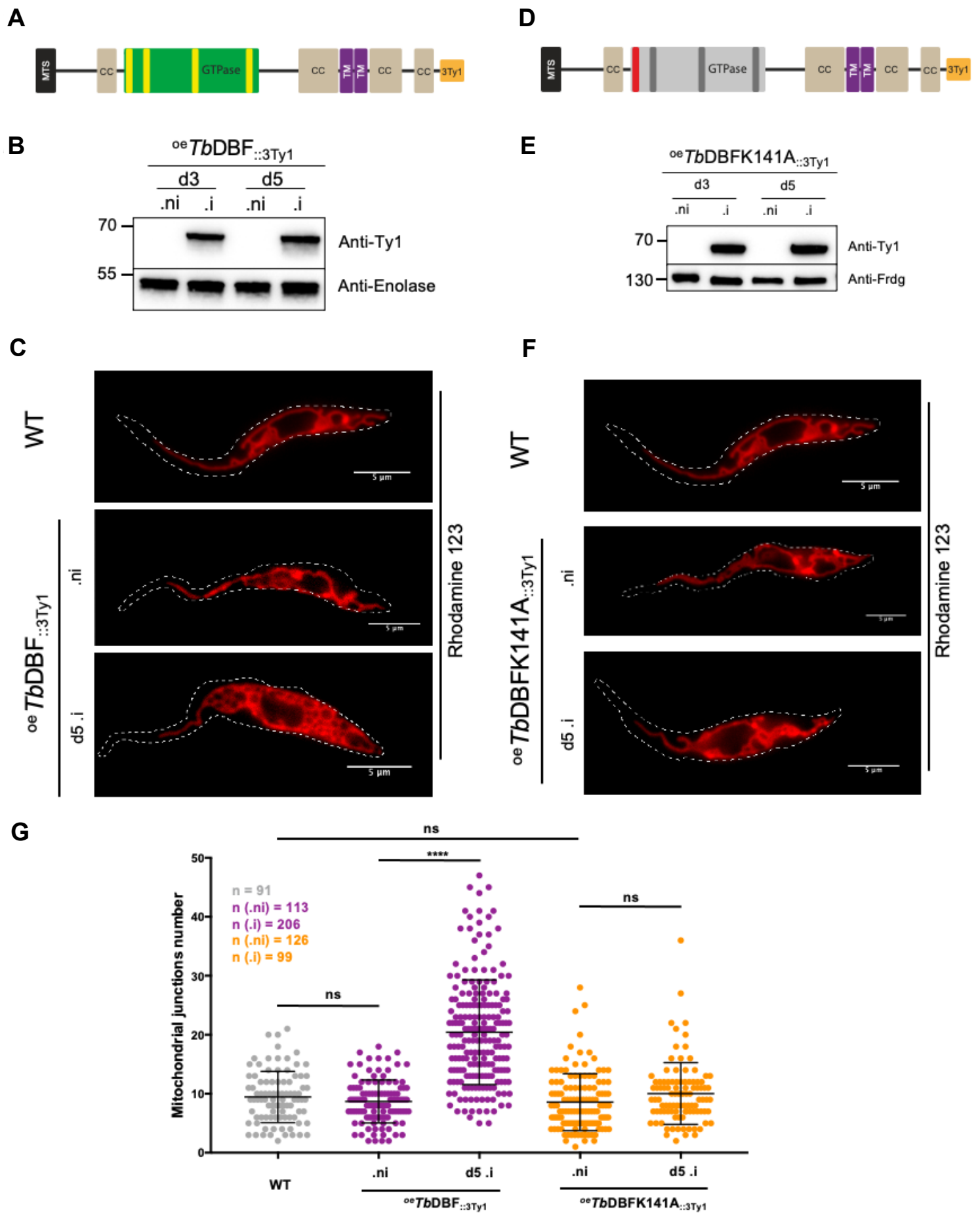
Figure 5 - Overexpression of _Tb_DBF and GTPase mutant. (A) Schematic representation of overexpressing _Tb_DBF protein tagged with 3Ty1 peptide at C-terminus of the protein (^oe^_Tb_DBF::3Ty1). **(B)** Western blotting of whole-cell extracts of _T. brucei_ PCF overexpressing _Tb_DBF::3Ty1 cells. Non-induced (ni) and induced (i) cells after 3 to 5 days (d3 and d5) were revealed with an anti-Ty1 antibody. Antibody directed against Enolase protein (Eno) was used as loading control. **(C)** Mitochondrial structure analysis using rhodamine 123 staining on living cells; mitochondrial structure of PCF WT and PCF ^oe^_Tb_DBF::3Ty1 cells before (ni) and 5 days after (i) tetracycline induction. **(D)** Schematic representation of overexpressing _Tb_DBFK141A::3Ty1 mutant protein tagged with 3Ty1 peptide at the C-terminus of the protein (^oe^_Tb_DBFK141A::3Ty1). **(E)** Western blotting of whole-cell extracts of _T. brucei_ PCF overexpressing _Tb_DBFK141A::3Ty1 cells; (ni) non-induced and (i) induced cells for 3 or 5 days (d3 and d5). Antibody directed against glycosomal Fumarate reductase protein (Frdg) was used as loading control. **(F)** Mitochondrial structure analysis using rhodamine 123 staining on living cells; mitochondrial structure of PCF WT and PCF ^oe^_Tb_DBFK141A::3Ty1 cells before (ni) and 5 days after (i) tetracycline induction. **(G)** quantification of mitochondrial junctions number using Rhodamine 123 microscopy images. Mitochondrial junctions number: WT, 9.4 ± 4.3; .ni ^oe^_Tb_DBF::3Ty1 8.7 ± 3.6; .i ^oe^_Tb_DBF::3Ty1 20.4 ± 8.9; .ni ^oe^_Tb_DBFK141A::3Ty1 8.6 ± 4.8 and .i ^oe^_Tb_DBFK141A::3Ty1 10 ± 5.2. Statistic : t test - Confidence interval 95% - P-value style : 0.1234 (ns); 0.0332 (*); 0.0021 (**); 0.0002 (***); <0.0001 (****).
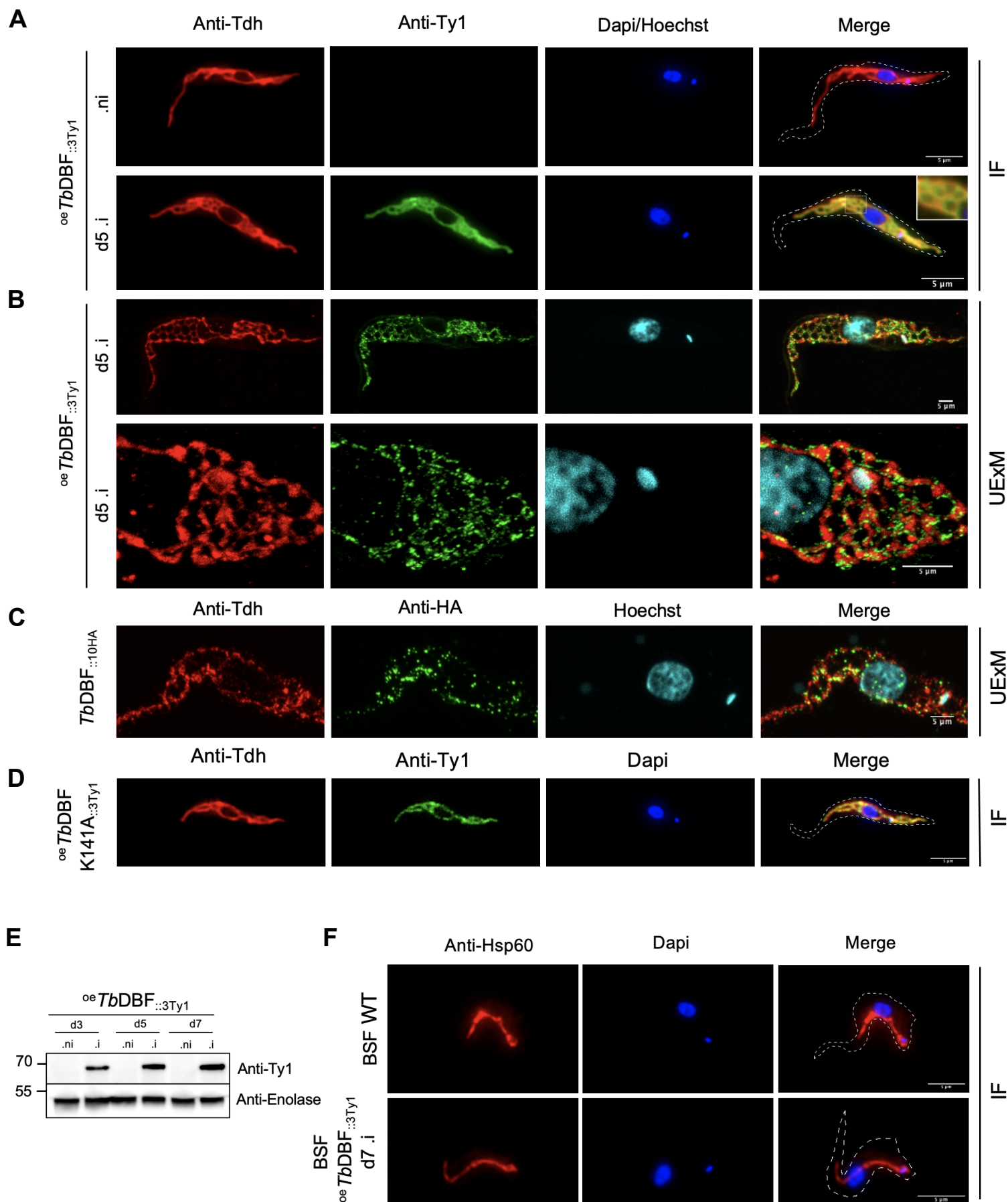
Figure 6 - Overexpression of *Tb*DBF and GTPase mutant. Subcellular localization of ^{oe}TbDBF$_{::3Ty1}$ in PCF by immunofluorescence and Ultra Expansion Microscopy (UExM); Colocalization of ^{oe}TbDBF$_{::3Ty1}$ (anti-Ty1 antibody) with matrix mitochondrial Threonine dehydrogenase (Anti-Tdh antibody) was analyzed by standard immunofluorescence **(A)** and by UExM with an expansion factor of ~4.4 **(B)**, after 5 days induction (d5.i). **(C)** Subcellular localization of *Tb*DBF$_{::10HA}$ in PCF analyzed by UExM. **(D)** Subcellular localization of ^{oe}TbDBFK141A$_{::3Ty1}$ in PCF analyzed by standard immunofluorescence. **(E)** Western blotting of whole-cell extracts of *T. brucei* BSF overexpressing *Tb*DBF$_{::3Ty1}$ cells. Non-induced (ni) and induced (i) cells after 3 to 7 days (d3, d5 and d7) were revealed with an anti-Ty1 antibody. Antibody directed against Enolase protein (Eno) was used as loading control. **(F)** Subcellular localization of ^{oe}TbDBF$_{::3Ty1}$ in BSF by immunofluorescence. Antibody directed against Hsp60 was used to label and visualized mitochondrial shape in wild type and *Tb*DBF$_{::3Ty1}$ overexpressing cells.
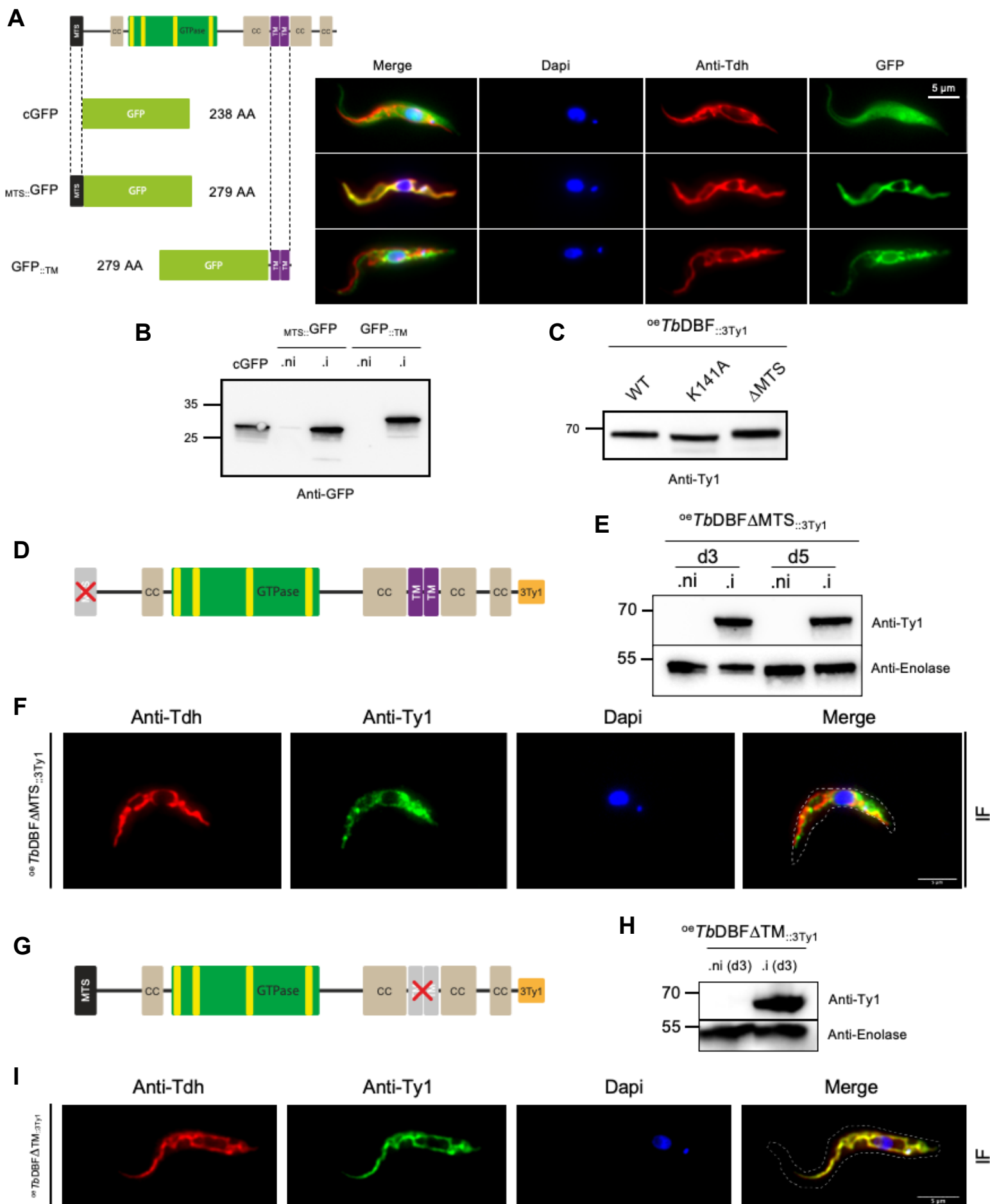
Figure 7 - Role of *Tb*DBF domains. (A) Localization of the GFP according to the different tags fused. Colocalization by standard immunofluorescence of GFP with matrix mitochondrial Threonine dehydrogenase (Anti-Tdh antibody) after 5 days induction. MTS, mitochondrial targeting signal; TM, transmembrane domains. **(B)** Western-blot analysis of GFP expression. cGFP, constitutive and cytosolic GFP. Non-induced (ni) and induced (i) cells after 5 days. **(C)** *Tb*DBF size analysis by western-blot using anti-Ty1 antibody. **(D)** Schematic representation of N-terminus truncated *Tb*DBF protein (first 41 amino acids) tagged with 3Ty1 peptide at the C-terminus of the protein (*oeTb*DBFΔMTS::3Ty1). **(E)** Western blotting of whole-cell extracts of *T. brucei* PCF overexpressing *Tb*DBFΔMTS::3Ty1 cells; (ni) non-induced and (i) induced cells for 3 or 5 days (d3 and d5). **(F)** Subcellular localization of *oeTb*DBFΔMTS::3Ty1 in PCF after 5 days induction. Colocalization of *oeTb*DBFΔMTS::3Ty1 (anti-Ty1 antibody) with matrix mitochondrial Threonine dehydrogenase (Anti-Tdh antibody) analyzed by standard immunofluorescence. **(G)** Schematic representation of truncated transmembrane domains of *Tb*DBF protein (45 amino acids) tagged with 3Ty1 peptide at the C-terminus of the protein (*oeTb*DBFΔTM::3Ty1). **(H)** Western blotting of whole-cell extracts of *T. brucei* PCF overexpressing *Tb*DBFΔTM::3Ty1 cells; (ni) non-induced and (i) induced cells for 3 days. **(I)** Subcellular localization of *oeTb*DBFΔTM::3Ty1 in PCF after 5 days induction, analyzed by standard immunofluorescence.
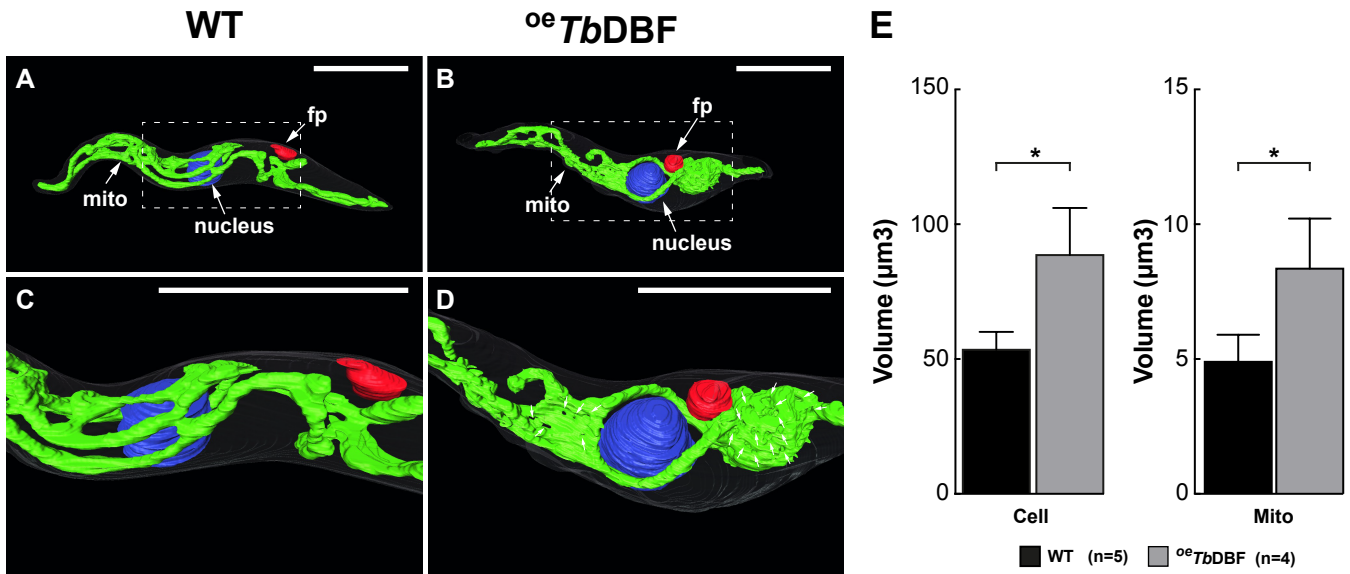
Figure 8 - Surface rendering of segmented PCF and determination of cell, nucleus and mitochondrion volumes using SBF-SEM. (A/B) Surface rendering of a segmented PCF (WT and ^{oe}TbDBF) showing the cell body (transparency), nucleus (blue), mitochondrion (green), and flagellar pocket (red). **(C/D)** Magnified view of the region boxed in A and B. Small arrows indicate mitochondria-free spaces in the mitochondrial network. The scale bar represents 5 µm. **(E)** Changes in the mean volumes of the cell and mitochondria. The n values are indicated on the right side of the legend. Volume in µm3, cell: WT 53.4±6.6, ^{oe}TbDBF 88.6±17.5; mitochondrion: WT 4.9±1, ^{oe}TbDBF 8.3±1.9. Statistic : t test - Confidence interval 95% - P-value style : 0.1234 (ns); 0.0332 (*); 0.0021 (**); 0.0002 (***); <0.0001 (****).
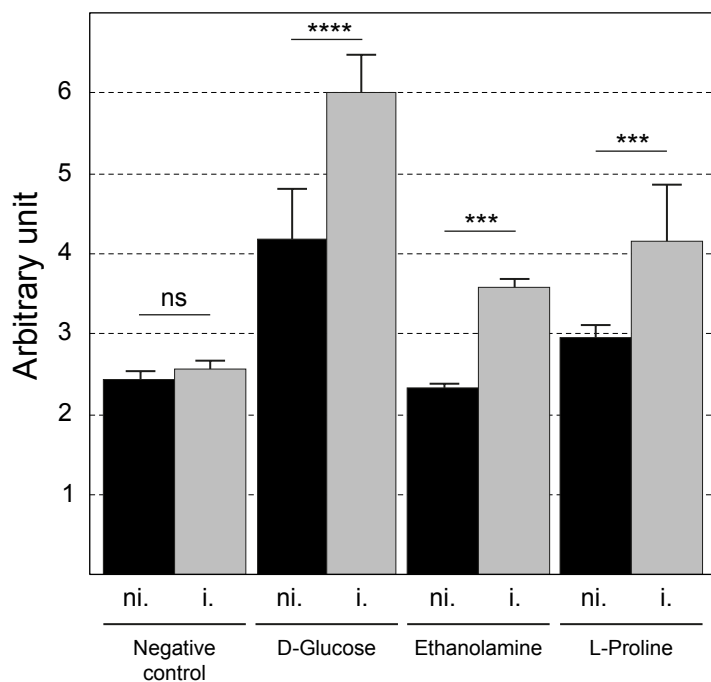
Figure 9 - Carbon sources used in cells overexpressing *oeTb*DBF::3Ty1. The metabolic pathway activities are assayed using a colorimetric reagent that measures redox production when a cell oxidizes a substrate (Biolog Phenotype MicroArrays™). Non-induced (black) and induced (grey) cells were incubated for 18 hours at 27°C with various substrates and redox production was measured by an endpoint absorbance at 590 nm. Only the 3 carbon sources showing significant variation are presented among the 119 molecules used. All the molecules (carbon and nitrogen sources) are show in Figure S11. The negative control corresponds to an absence of carbon sources. Statistic : Two way ANOVA - Confidence interval 95% - P-value style : 0.1234 (ns); 0.0332 (*); 0.0021 (**); 0.0002 (***); <0.0001 (****), n=3.
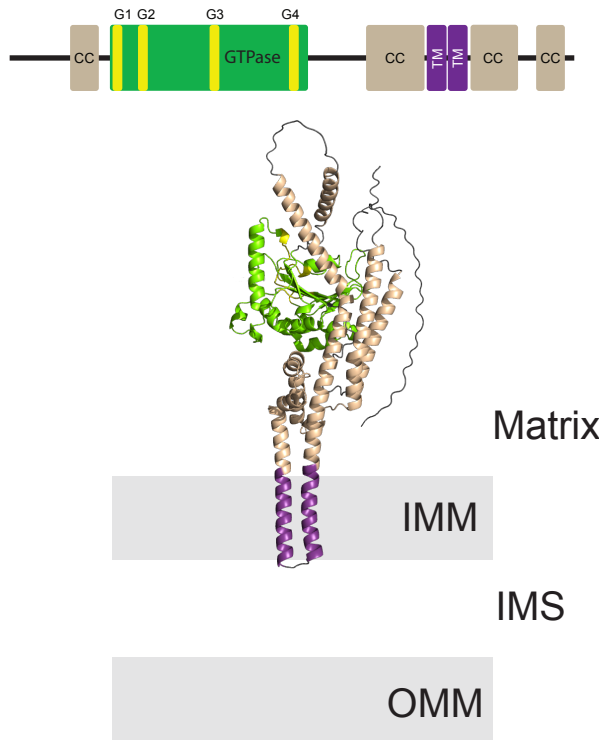
Figure 10 – Proposed submitochondrial localization and membrane topology of *Tb*DBF. Predicted structure of *Tb*DBF, from AlphaFold protein structure database. *Tb*DBF was embedded in mitochondrial inner membrane (IMM). The color coding correspond to the predicted secondary structure depicted on the top of the figure. The N-terminus MTS was not displayed as it is cleaved. The AlphaFold model score of *Tb*DBF is between confident to very high for most of the structured regions (https://alpha-fold.ebi.ac.uk/entry/Q57XN3).

Supplemental material

Figure S1 shows alignment between human and trypanosome mitochondrial dynamin-

related proteins.

Figure S2 shows alignment of various kineoplastids DBF proteins.

Figure S3 shows alignment between _Tb_DBF and various eukaryotes and prokaryotes.

Figure S4 shows growth curves of parental, over-expressing and mutant cells.

Figure S5 shows the inactivation of _Tb_DBF expression by CRISPR/Cas9 system.

Figure S6 shows the down-regulation of _Tb_DBF expression by RNAi.

Figure S7 shows results of the ImageJ plugin on rhodamine-stained cells.

Figure S8 shows the level of overexpression of different _Tb_DBF variants.

Figure S9 shows mitochondrial localization of _Tb_DBF by EM.

Figure S10 shows similar localization of GFP$_{::TM}$ and ^{oe}_Tb_DBFΔMTS.

Figure S11 shows carbon, energy and nitrogen sources used in cells overexpressing

_Tb_DBF.

Table S1 shows results from BLASTp analysis of several identified organisms.

Table S2 shows all the primers and guide RNA used in this study.

Table S3 shows all the antibodies used in this study.

Materials and Methods: MMS1 described the ImageJ macro.